A Method for Measuring Optical Distortion in Curved Optical Surfaces using Moiré Interferometry

Mark A. Nurge
KSC Applied Physics Lab, Kennedy Space Center, Florida

Robert C. Youngquist
KSC Applied Physics Lab, Kennedy Space Center, Florida

Annelisa B. Esparza
KSC Applied Physics Lab, Kennedy Space Center, Florida

June 2022

NASA STI Program...in Profile

Since its founding, NASA has been dedicated to the advancement of aeronautics and space science. The NASA scientific and technical information (STI) program plays a key part in helping NASA maintain this important role.

The NASA STI Program operates under the auspices of the Agency Chief Information Officer. It collects, organizes, provides for archiving, and disseminates NASA's STI. The NASA STI Program provides access to the NASA Aeronautics and Space Database and its public interface, the NASA Technical Report Server, thus providing one of the largest collection of aeronautical and space science STI in the world. Results are published in both non-NASA channels and by NASA in the NASA STI Report Series, which includes the following report types:

- TECHNICAL PUBLICATION. Reports of completed research or a major significant phase of research that present the results of NASA programs and include extensive data or theoretical analysis. Includes compilations of significant scientific and technical data and information deemed to be of continuing reference value. NASA counterpart of peer-reviewed formal professional papers, but having less stringent limitations on manuscript length and extent of graphic presentations.

- TECHNICAL MEMORANDUM. Scientific and technical findings that are preliminary or of specialized interest, e.g., quick release reports, working papers, and bibliographies that contain minimal annotation. Does not contain extensive analysis.

- CONTRACTOR REPORT. Scientific and technical findings by NASA-sponsored contractors and grantees.

- CONFERENCE PUBLICATION. Collected papers from scientific and technical conferences, symposia, seminars, or other meetings sponsored or co-sponsored by NASA.

- SPECIAL PUBLICATION. Scientific, technical, or historical information from NASA programs, projects, and missions, often concerned with subjects having substantial public interest.

- TECHNICAL TRANSLATION. English-language translations of foreign scientific and technical material pertinent to NASA's mission.

Specialized services also include organizing and publishing research results, distributing specialized research announcements and feeds, providing information desk and personal search support, and enabling data exchange services.

For more information about the NASA STI Program, see the following:

- Access the NASA STI program home page at http://www.sti.nasa.gov

- E-mail your question to help@sti.nasa.gov

- Phone the NASA STI Information Desk at 757-864-9658

- Write to:
  NASA STI Information Desk
  Mail Stop 148
  NASA Langley Research Center
  Hampton, VA 23681-2199

A Method for Measuring Optical Distortion in Curved Optical Surfaces using Moiré Interferometry

Mark A. Nurge
KSC Applied Physics Lab, Kennedy Space Center, Florida

Robert C. Youngquist
KSC Applied Physics Lab, Kennedy Space Center, Florida

Annelisa B. Esparza
KSC Applied Physics Lab, Kennedy Space Center, Florida

June 2022

Acknowledgments

Abstract

In FY2020, KSC's Applied Physics Lab created a computer based image processing system to allow inspection of the new visors being developed for the Artemis Program. This system was based on an ASTM standard where the distortion of an image is used to determine the optical aberrations in a visor, but this approach is restricted to small fields-of-view (small areas of the visor) and is limited in its ability to reliably detect and measure distortion. From our experience with flat surface inspection, we know that other optical techniques can offer higher sensitivity and accuracy. [1] This memorandum describes a method to model and measure the distortion in curved optical surfaces using moiré interferometry. We were able to apply this process to examine samples of the xEMU Artemis astronaut helmets. Design details are provided along with examples to illustrate performance.

Contents

1   Introduction

The primary methods used for optical window inspection employ some form of image comparison. One of the key measurement parameters is optical distortion, which is defined as the spatial variation that will appear to occur to a visual target when seen by an observer through a given section of material. The military still specifies ASTM procedures (e.g., ASTM-F2156-17) [2] that require photography of an image taken of a grid-like target both with and without the curved surface in place. Typically, this is used to look at what a pilot will see through an aircraft canopy. The before and after images are analyzed to determine the slope and positional changes of the grid points between the two images.

Management identified a need to characterize the distortion in terms of diopter variations in newly manufactured Artemis spacesuit helmets. There was no off the shelf tool to automate the inspection process. Thus, we developed a method of performing this measurement using a backlit grid of dots, a high resolution digital lab camera, and image acquisition/machine vision software. We were able to achieve accuracy required by the customer but with little room to spare. In order to achieve higher accuracy, we began to investigate and eventually developed a system based on moiré interferometry using a digital camera, light source, opal glass, Ronchi ruling, spherical mirror, computer controllable rotary stages, one-inch Thorlabs rails, and associated hardware. The resulting system is shown in Figure 1. A custom designed mount was fabricated to hold the camera, light source, opal glass, and Ronchi ruling. The resulting mount is shown in Figure 2. The customer requested that we identify areas of the visor that had more than a 0.125 diopter change from the surrounding surface. This made it desirable to have a noise floor of less than 0.0125 diopters. Our approach has resulted in a noise floor of about 0.0018 diopters.

The sections below provide a review of the distortion definitions and the computations used for the moiré interferometry method. Details are provided on the hardware construction to hold and manipulate the visor and the associated inspection equipment. A modeling program was created in Mathematica to help in construction of this system that provides estimates of the optical performance along with scan coordinates and key reference parameters for the image analysis program. This software is discussed along with how it may be used to adjust the system for use with inspection of other curved optics. A section is devoted to the software design that provides the translation of the visor and image capture. Next, details are provided on the image processing and algorithm applied to compute the distortion from the digital scans. Lastly, a discussion is presented covering the performance metrics of the system and some comparisons with the prior method.
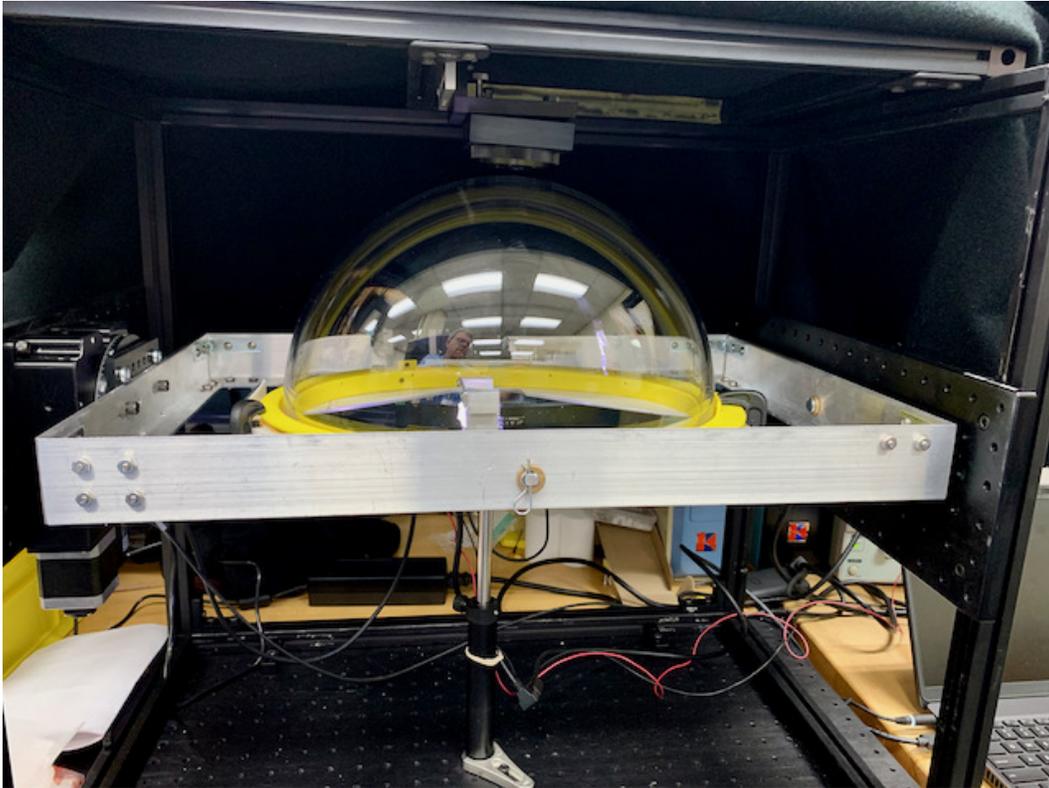
Figure 1: A photo showing the full system with a sample test part. The main rotary stage is visible along the left hand side of the image. The camera, light source, opal glass, and Ronchi ruling are in a custom designed mount in the center. The spherical mirror is in a mount located at the top center of the photo.

Figure 2: A photo showing the custom designed optics mount that attaches to the camera and contains the light source, opal glass, and Ronchi ruling. The mount is designed so that Ronchi ruling may easily be rotated 90 degrees by hand.

2 A Simplified System Model Using Moiré Interferometry Leading to Distortion Estimates from Imagery

In another section of this report a sophisticated model is described that predicts the moiré pattern observed for the visor. This forward model is important for verifying the performance of the system, but does not provide a means by which given imagery can be used to yield distortion estimates. To achieve that a simplified model is needed, one that lacks the fidelity of the forward model and is only applicable over a limited range of operation, but provides enough structure to yield a relationship between the observed imagery and the corresponding distortion.

Much of the analysis below is a modified version of the analysis provided in NASA Technical Memorandum, NASA/TM-2015-218822. [1]

2.1 The system without a visor present

Begin with the system sketched in Figure 3. A light source generates a uniform illumination that is launched through a Ronchi ruling with line spacing, f. This light propagates out to a concave spherical mirror with radius of curvature given by R. The light reflects from the mirror at some angle, φ, about the mirror normal and heads back to the Ronchi ruling, hitting it at a distance y above the mirror center-line. This light then enters the camera producing an image.
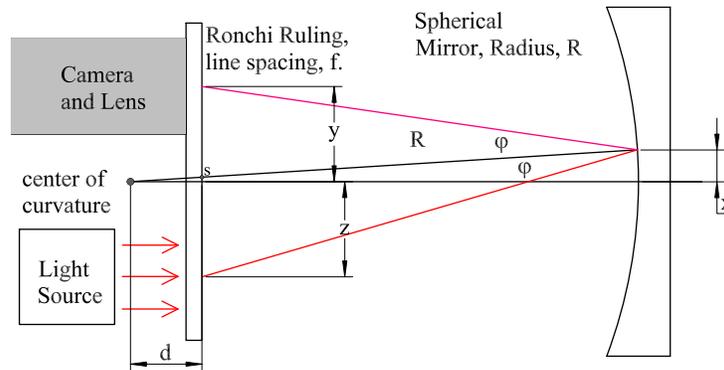
Figure 3: A sketch showing the parameters used to model the system.

If the Ronchi ruling were located at a distance R from the mirror, this would be a classic Schlieren optical system, with one large fringe filling the field of view. Such a configuration is very sensitive to small changes in the optical path and can even image variations in the index of refraction of the atmosphere between the ruling and the mirror, but this is too sensitive for the current application. Fortuitously, the sensitivity of this optical system to deflections of the optical rays can be reduced

by moving the Ronchi ruling towards (or away) from the mirror (this change in sensitivity will be quantified below). In Figure 3 this shift of the Ronchi ruling from the mirror center of curvature is given by the parameter, d.

In this analysis, assume that the camera iris is closed down so that that camera is only looking through one open line on the Ronchi ruling. Doing this simplifies the development and additional open lines on the ruling can be added by following the same development as shown below. So let the distance y be the distance from the system center-line to this open line on the Ronchi ruling that the camera is looking through. Figure 1 shows this ray as a red line, representing a possible path for a beam of light starting from the light source, reflecting off of the mirror and then reaching the Ronchi ruling opening that the camera is looking through. This single optical path represents light emerging a distance z below the system center-line and reflecting off of the mirror a distance x on the mirror from the system center-line.

The distance x corresponds to a location within the camera's field of view. Assume for the moment that it is chosen such that the camera sees maximal light when looking at that height on the mirror, i.e. that the red ray begins at an opening on the Ronchi ruling from which light is emerging. An important question is, How far up or down in the camera's image of the mirror is the next bright line. Equivalently, what Δx, corresponds to a Δz equal to the Ronchi ruling spacing, f.

Figure 3 is not to scale. In the actual system the angles are small because the mirror radius, R, is much larger than the parameters, x, y, or z. Consequently, it can be assumed that the triangle corresponding to the red ray, with a base formed by the Ronchi ruling, is approximately an isosceles triangle, bisected by the angle φ. This bisection follows the mirror radial line from the offset distance x on the mirror back to the center of curvature, passing through the Ronchi ruling at a location noted by a small s in Figure 3. Since this is the bisection point at the base of the triangle,

$$y - s = z + s \tag{1}$$

where y and z are positive and s can be positive or negative. Now, by equivalent triangles

$$\frac{s}{d} = \frac{x}{R} \tag{2}$$

and recalling that y is fixed, solving for the z yields

$$z = y - 2s = y - \frac{2xd}{R} \tag{3}$$

Recalling that y is fixed, we obtain

$$f = \Delta z = -\frac{2d}{R}\Delta x \qquad \rightarrow \qquad \Delta x_{\text{one line}} = -\frac{fR}{2d}. \tag{4}$$

This shows that the line spacing of the moiré image can be scaled by adjusting the distance d, Note that if $d = 0$ then there are no lines, just one large fringe. As an example, in the present system the mirror has a radius of curvature equal to 8 inches and a diameter of 2 inches. The Ronchi ruling has a line spacing of 0.01 inches. If the Ronchi ruling is located such that $d = 1/2$ an inch then we expect to see a line in the imagery every 0.08 inches, or about 25 lines over the two inch

diameter window. Figure 4 shows the image obtained where there are 26 lines across the window, which is within the tolerance of measurement of d.

(a) vertical ruling

(b) horizontal ruling
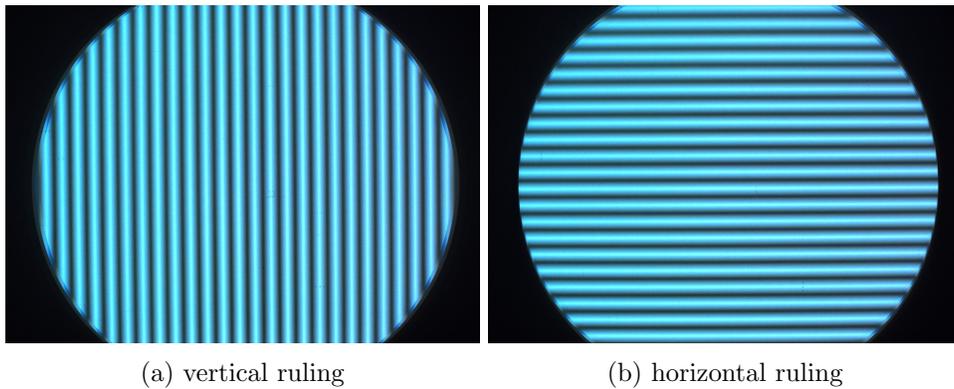
Figure 4: An image from the visor metrology system without a visor present and the Ronchi ruling oriented vertically and horizontally.

2.2 The system with an ideal visor present

Figure 5 shows a sketch of the system with the visor present. The visor is approximately a half oblate spheroid with major axis equal to 7.05 inches and minor axis equal to 5.55 inches. It is located within an inch of the mirror as shown in Figure 5, such that the center of curvature of the major arc is approximately in the same location as the mirror center of curvature.
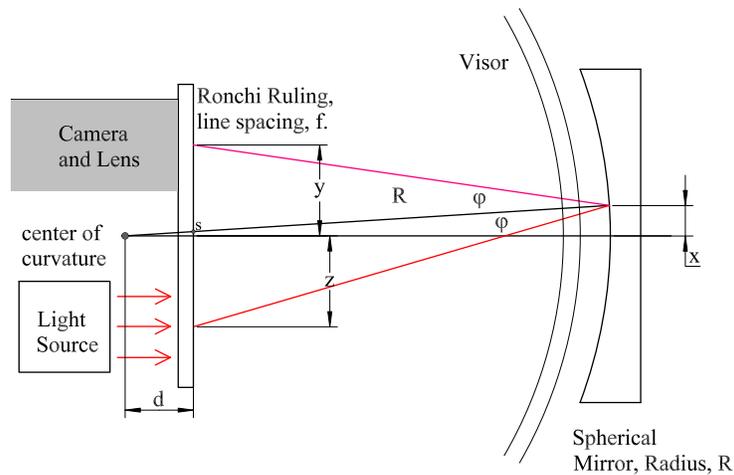
Figure 5: A sketch showing the system with a visor present.

The more sophisticated model traces the light rays and accounts for the different curvatures, however, that model has shown minimal effect on the imagery due to

7
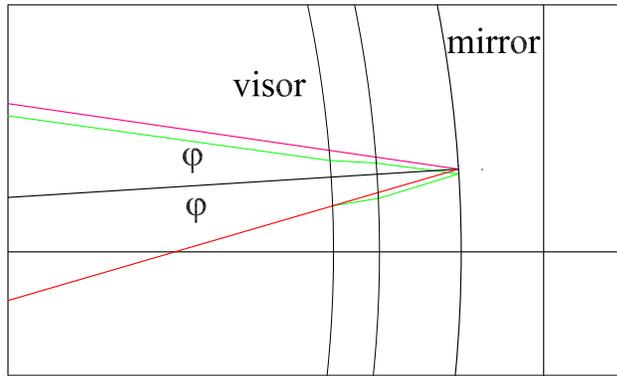
Figure 6: Approximate deflection of the light rays due to the visor.

the presence of a "perfect" visor, i.e., one without defects. A similar result is seen here. Consider Figure 6, where a ray from the light source is traced out to the visor. The red line shows the path if the visor were not present and the green ray shows the ray being refracted, reflected off of the mirror, and then refracted again. If the shift due to the refraction is small, then the returning green ray will be parallel to the red ray and the effect of the visor will be a shift in the imagery. It was shown in TM NASA/TM-2015-218822 that a flat plastic sheet caused the line spacing to be slightly smaller, adding about a full line across the image, but with the visor curvature as shown this effect, if present, is small. Also, efforts have been made to minimize the angle φ, which will cause the light rays to impinge on the visor at a nearly normal angle of incidence, further minimizing the effect of the visor on the imagery. Consequently, for the approximate analysis being described here it will be assumed that a perfect visor has no effect on the imagery.

(a) -20 degrees (b) +20 degrees
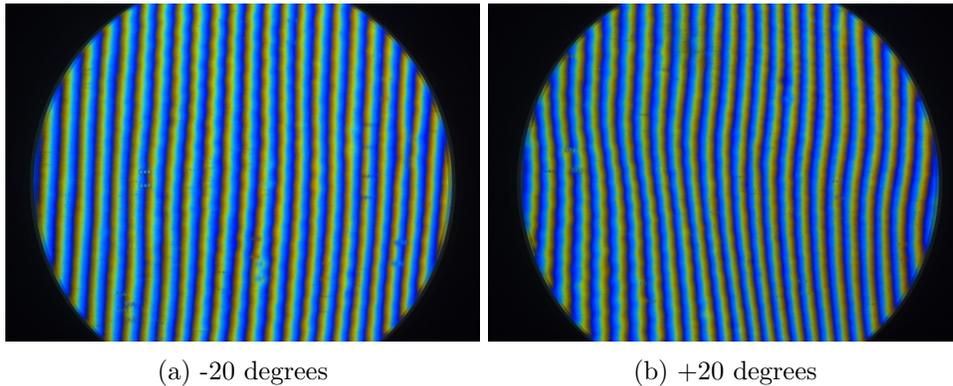
Figure 7: These are images taken through two locations on the visor, +20 and -20 degrees from normal.

Figure 7 shows the imagery taken through two locations on the visor, plus 20

8

and minus 20 degrees from normal. The minus 20 degree image has about 24 lines and the plus 20 degree image has just over 25 lines. These are both less than the 26 lines seen in the no visor image shown in Figure 2a, but not by much, and support the assumption for this approximate analysis that the imagery effect of an ideal visor can be ignored.

2.3 The effect of a visor deformation on the imagery

This section will develop the expressions and algorithms allowing variations in the imagery to be converted to distortion measurements. However this is restricted to images where the effect of the visor is to cause the moiré lines to follow a curved paths, such as those shown in Figure 8, horizontal and vertical images taken from the top center of a visor. This restriction implies that the system has been configured, by changing the displacement of the Ronchi ruling (distance d), to adjust the sensitivity. If d is made too small for a given distortion the imagery can yield lines too compressed to see, closed loops, and even apparent discontinuities in the lines. Increasing d reduces the system sensitivity, but also yields imagery that can be analyzed by following the curves of the lines. Also, the analysis provided here is not meant to determine large smooth variations in the visor imagery, but is limited to localized areas whose effect can be seen in the mirror (currently 2 inches in diameter). A future upgrade may allow stitching of the imagery to allow larger scale issues to be quantified.

(a) horizontal (b) vertical
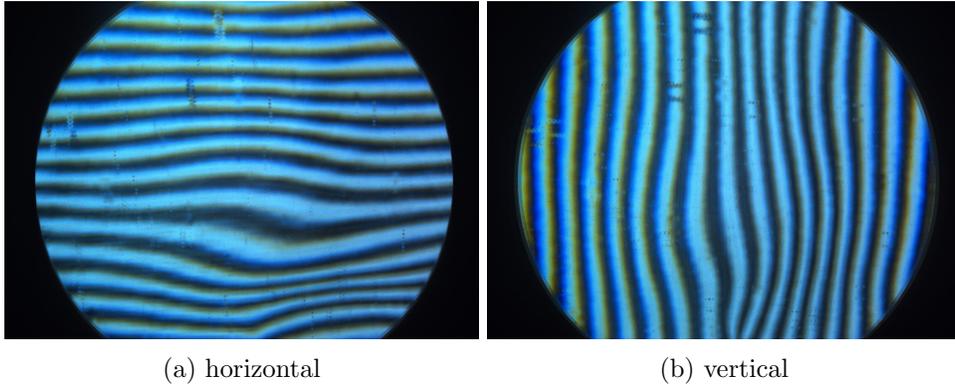
Figure 8: Imagery looking through the top center of a visor with the Ronchi ruling horizontally positioned and then vertically positioned.

2.3.1 Distortion

The goal of the system is to map distortion across the visor, locating regions that will impair visibility above some threshold. To quantify this, it is important to first recall the various definitions of distortion (see NASA/TM-2015-218822 for details):

$$D = \frac{d\alpha}{dx} = -\frac{n-1}{R} = \frac{1}{F} = \frac{d^2\sigma}{dx^2} \tag{5}$$

9

where α is the angular deviation from normal experienced by a ray traveling through the visor (note that we will account for the double pass that the light makes through the visor later in the analysis). n is the index of refraction of the visor and R is the radius of curvature of the deformation on the visor assuming only one side of the visor is deformed. F is the equivalent focal length of the deformation and σ is the optical path length through the visor.

Let's consider an example. Let the visor have a bump, modeled as a Lorentzian, on its far side so that the total optical path length through the visor is given by

$$\sigma[x, y] = \frac{b}{1 + (x^2 + y^2)/a^2} + \sigma_0 \tag{6}$$

where σ_0 is the optical path length through the ideal visor, which is assumed to be a constant, and where b and a are constants with units of length. Note that b contains a factor of $n - 1$ since adding a physical bump of material with index n removes the same physical distance in air. Recall that the radius of curvature of a lens is related to its focal length (assuming the lens is in air and that one side of the lens does not refract the light) by

$$\frac{1}{F} = -\frac{n - 1}{R} \tag{7}$$

(this is a restatement of 5). Now recall that the radius of curvature is the reciprocal of the curvature, found by taking the second derivative of the optical path length function (note that this assumes that the curvature is measured at a functional peak where the first derivative is zero). So, at its peak (near $x = 0$ and $y = 0$), the second derivative of the bump is the distortion of the bump, i.e.

$$D_{\text{bump}} = \frac{d^2\sigma}{dx^2} = -2a^2 b \frac{a^2 - 3x^2 + y^2}{(a^2 + x^2 + y^2)^3} \approx -\frac{2b}{a^2}, \tag{8}$$

a relatively simple result.

At present the pass/fail criteria on the visor is a distortion of 0.125 m^{-1} and since the mirror is 2 inches in diameter it would be convenient to make this bump roughly 1 inch in diameter. So set $a = 6.35$ mm and then $b = 2.5 \times 10^{-6}$ m yields the desired distortion. The bump is only 2.5 microns in height a very small distance, yet yielding a significant optical effect. Figure 7(a) shows a plot of the bump where all if the units are in millimeters, so this plot covers about a 2 inch by 2 inch area.

Figure 9(b) shows the first derivative of the bump in x indicating a rising slope and then a rapid transition to a negative slope on the other side of the bump's peak. The slopes are in units of radians and have a peak value of about 0.00027 radians. Figure 10 shows the second derivative of the bump in x and in y where x and y are in millimeters and the z axis is in units of inverse meters, or diopters. The bump is radially symmetric and the second derivatives consequently have the same shape, but along different axes. These second derivatives map the distortion caused by the bump and have peak values of -0.125 meters, by design.

It should be pointed out that the bump has a peak distortion in x of 0.125 diopters and a peak distortion in y of 0.125 diopters, but that these should not be

(a) bump

(b) first derivative of the bump in x
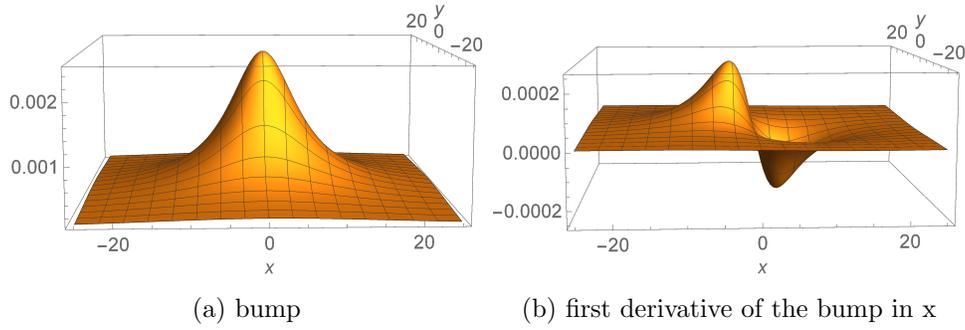
Figure 9: The bump and its first derivative.

(a) second derivative of the bump in x

(b) second derivative of the bump in y
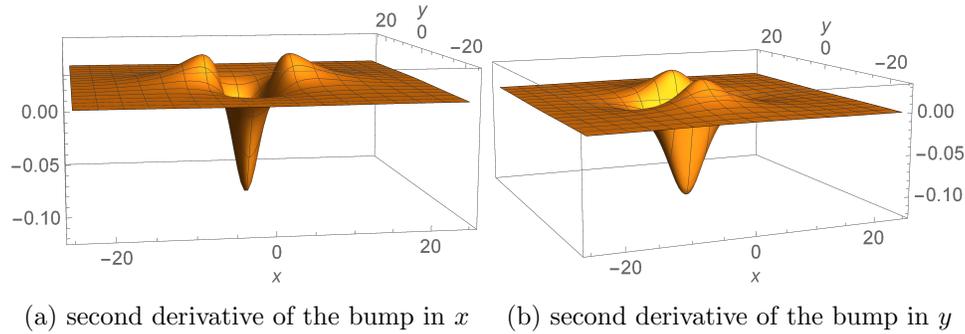
Figure 10: The second derivatives of the bump in x and in y

added. NASA/TM-2015-218822 states that the total distortion is the Laplacian of the bump, but this would yield a distortion of 0.25 diopters and that is not correct. Neither should they be added as components of a vector (root of the sum of the squares). They are simply distortions in different directions and are independent of each other.

Now consider Figure 11, a stepping stone to the moiré plots that result from imaging through the visor. This figure consists of horizontal lines for each value of x stepped by 1.5 mm from the center, plotted along the y axis, with 10,000 times the angular deviation (shown in Figure 7b) added at each value of x and y. Mathematically,

$$x_i + 10,000 \frac{d\sigma}{dx}(x_i, y) \quad \text{for} \quad x_i = 0 \pm i1.5\text{mm} \quad i \in (-6, 6) \tag{9}$$

The factor of 10,000, converting from radians to millimeters, is arbitrary and was chosen only to scale the angular deviations such that they were visible in the plot. Curved lines, such as these, appear in the actual imagery, but the conversion factor will be determined from system parameters and is developed below.

The goal of the moiré imaging system is to map the distortion of the visor, i.e. to find $d^2\sigma/dx^2$ (and the y derivative) from imagery like that shown in Figure 11. Possible ways to do this are:

1. If the x_i spacing is known (discussed above), then it can be subtracted out,

11
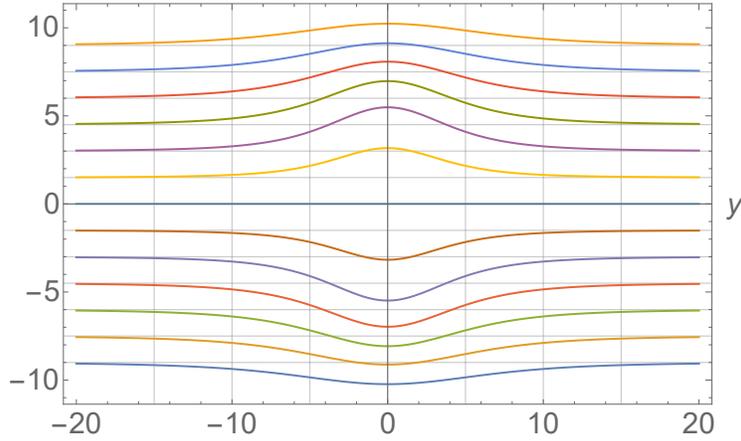
Figure 11: This is a plot of the angular deviation in x as a function of x and y displayed by plotting a horizontal line every $\Delta X = 1.5$ mm and then adding 10,000 times the angular deviation in radians to that value of x and plotting it as a function of y.

leaving $d\sigma/dx$ times a yet to be determined constant. Assuming the constant is known, it can be factored out and the derivative in x taken.

2. Assuming the spacing $x_{i+1} - x_i$ is known, then adjacent lines can be subtracted leaving

$$x_{i+1} - x_i + 10,000 \left(\frac{d\sigma}{dx}(x_{i+1}, y) - \frac{d\sigma}{dx}(x_i, y) \right) \tag{10}$$

Dividing by the known spacing yields

$$1 + 10,000 \frac{\left(\frac{d\sigma}{dx}(x_{i+1}, y) - \frac{d\sigma}{dx}(x_i, y) \right)}{x_{i+1} - x_i} \approx 1 + 10,000 \frac{d^2\sigma}{dx^2} \tag{11}$$

as an example, consider the $y = 0$ vertical line in Figure 9 and look at the $x = 0$ and the $x = 1.5$ mm lines. The spacing is known to be 1.5 mm and the $x = 1.5$ mm line reaches a peak on the $y = 0$ axis of about 3.17. So Eqn 10 becomes

$$x_{i+1} - x_i + 10,000 \left(\frac{d\sigma}{dx}(x_{i+1}, y) - \frac{d\sigma}{dx}(x_i, y) \right) = 1.5 \, \text{mm} + 1.67 \, \text{mm} \tag{12}$$

yielding

$$10,000 \frac{\left(\frac{d\sigma}{dx}(x_{i+1}, y) - \frac{d\sigma}{dx}(x_i, y) \right)}{x_{i+1} - x_i} = 1.67 \, \text{mm}/1.5 \, \text{mm} \tag{13}$$

and an estimated distortion value near the origin of

$$\frac{d^2\sigma}{dx^2} \approx 0.00011 \, \text{mm}^{-1} = 0.11 \, \text{Diopters} \tag{14}$$

0.11 Diopters is not far from the design value of 0.125 Diopters.

12

2.4 System conversion from line deviation to angle

The final parameter needed to determine distortion from the imagery is the conversion from distance in the visor image to angle. In the example above a factor of 10,000 mm/radian was used, but this was arbitrary and an actual value is needed. Recall from the conversation above (see Eq. 4) that if the light at the visor is redirected to a spot on the Ronchi ruling, Δz, offset that the corresponding line in the imagery will shift by a distance Δx given by

$$\Delta x = \frac{\Delta z R}{2d} \tag{15}$$

The angular change in the direction of the light is given by $\phi = \Delta z/R$, so this becomes

$$\Delta x = \frac{R^2}{2d}\phi \tag{16}$$

So the conversion between ϕ and Δx in the present system is (25.4 mm/in)*(8 in)^2/(2*0.5 in)=1625 mm/radian. However, we need to determine yet how the light passing through the visor is deflected, i.e. we need to establish a relationship between α, the angular shift caused by the visor and ϕ, the angular shift in the light coming back from the mirror after passing through the visor twice.

Before proceeding, note that the light that passes through the visor and reflects off of the mirror, passes through the visor a second time at a different location. In the present system the Ronchi ruling is located about 7.5 inches from the mirror and the separation between the camera and the light source is about 1 inch. The visor is less than 1 inch from the mirror, so the two passes made by the light are about 0.13 inches apart. Consequently, the system will average distortions over this distance and it will be assumed for the analysis to proceed that any perturbation in the visor is smooth, with minimal variation, over distances of 0.13 inches.

During the project we often assumed that $\phi = 2\alpha$, simply assuming that two passes through the visor would double the angular shift caused by the visor. This turns out to be justifiable as seen in Figure 12. In this Figure, we assume that locally we can model the system as being flat. We could generalize this discussion to a curved visor and mirror where a small tilt is added to the locations where the light passes through the visor, and then find the deviations in the final angles, but for now will assume that the flat representation conveys the necessary physics.

Start with an incoming beam of light, shown by the red line with the arrow head. It pass through the visor and, in this flat case, would normally hit the window head on and bounce back along the same path that it came in on. Instead, tilt the back surface of the visor an angle θ, shown by the blue line. Now the light hits the interface at an angle θ, and is refracted by an angle $n\theta$ about the normal where n is the index. The deviation from the original path is given by α, the parameter we wish to know. Looking at the figure, $\alpha = n\theta - \theta = (n-1)\theta$.

The light then heads to the flat mirror at angle α, bounces off the mirror as shown, and then hits the visor at an angle relative to the visor normal given by $\theta - \alpha = (2 - n)\theta$. This light is refracted, moving closer to normal, at an angle of $(2 - n)\theta/n$ from it. The light passes through the visor, hitting the last surface
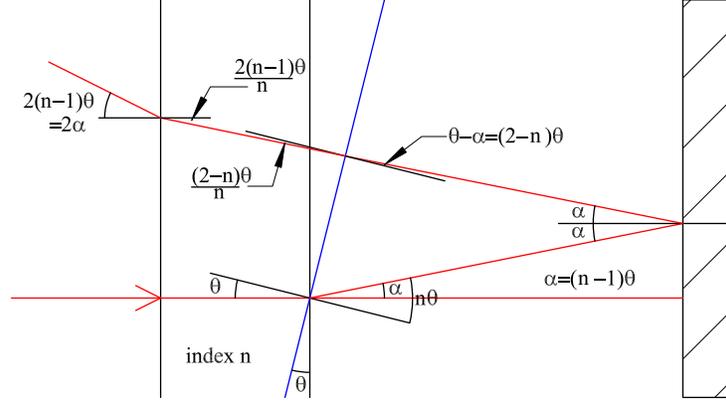
Figure 12: This is a ray trace to show the effect of passing through an aberration twice.

at an angle of $2(n-1)\theta/n$ from the normal to this surface, and is refracted to an angle of $2(n-1)\theta = 2\alpha$ from horizontal. This substantiates the assumption that the after passing through the visor twice that the light is deflected by two times α, i.e. $\phi = 2\alpha$. So the conversion between a shift in the imagery, Δx to the visor deflection angle, α, is given by

$$\Delta x = \frac{R^2}{d}\alpha \tag{17}$$

Using the system parameters this is $\Delta x = (3250\,\text{mm/radian})\,\alpha$.

2.5 Example

Now consider the images shown in Figure 6 above where the system is imaging the top center of a visor. The image in the vertical direction shows 16 lines across the 2 inch mirror, while the ideal visor should show 25-26. What this means is that there is an overall positive distortion across this 2 inch region causing the line spacing to be increased. Each line spacing is about 3.17 mm instead of 2.03, indicating an additional separation of 1.14 mm per line. So consider two adjacent lines, described as

$$\begin{aligned}
x_i + 3250\,\text{mm/rad}\,\alpha(x_i, y) &= c \\
x_{i+1} + 3250\,\text{mm/rad}\,\alpha(x_{i+1}, y) &= c + 3.17\,\text{mm}
\end{aligned} \tag{18}$$

where $x_{i+1} - x_i = 2.03$, the non-distorted line spacing. Subtracting these yields

$$2.03\,\text{mm} + 3250\,\text{mm/rad}\,(\alpha(x_{i+1}, y) - \alpha(x_i, y)) = 3.17\,\text{mm} \tag{19}$$

yielding

$$(\alpha(x_{i+1}, y) - \alpha(x_i, y)) = 0.35\,\text{mrad} \tag{20}$$

14

The two measurement points are separated by 3.17 mm, so the derivative, i.e. the distortion, D, is

$$D = \frac{\alpha(x_{i+1}, y) - \alpha(x_i, y)}{3.17\,\text{mm}} = 0.11\,\text{m}^{-1} = 0.11\,\text{Diopters.} \quad (21)$$

So the center top region of this visor has an effective focal length of about 9 meters, near the pass/fail mark of 0.125 Diopters.

There is an alternative way to do this calculation, which is worth developing for comparison. If a long focal length lens is placed in front of the mirror, it will change the effective radius of the mirror, and hence the line spacing. To calculate this, first recall that the focal length of the mirror, f_M, and the focal length of lens, $1/D$, can be added to find a new mirror focal length, f'_M,

$$\frac{1}{f'_M} = 2D + \frac{1}{f}_M \quad (22)$$

where the factor of 2 accounts for two passes through the lens. Now recall that the mirror radii are twice the focal lengths, yielding

$$\frac{1}{R'_M} = D + \frac{1}{R} \quad (23)$$

Now, rewrite the equation for the line spacing as

$$\Delta x_{\text{one line}} = \frac{f R'_M}{2(R'_M - t)} = \frac{f}{2(1 - \frac{t}{R'_M})} \quad (24)$$

where t is the distance from the Ronchi ruling to the mirror. Now, combine the last two equations to obtain

$$\Delta x_{\text{one line}} = \frac{f R'_M}{2(R'_M - t)} = \frac{f}{2(1 - tD - t/R)} \quad (25)$$

Now solve for the distortion, D, yielding

$$D = -\frac{1}{R} + \frac{1}{t} - \frac{f}{2\Delta x_{\text{oneline}} t} \quad (26)$$

If we assume that the distance t is 7.5 inches and that the line spacing is 0.08 inches, this equation yields a distortion of 0, as expected, since those parameters correspond to an ideal visor with no distortion. However, if we use the line spacing 3.17 mm (0.125 inches) from above we obtain a distortion of 0.003 inches^{-1}, or 0.118 m^{-1} or 0.118 Diopters, which is very close to the 0.11 Diopter value found above. The agreement between these two different processes substantiates the development of each.

3 Hardware Design



(a) Hinge up   (b) Hinge down
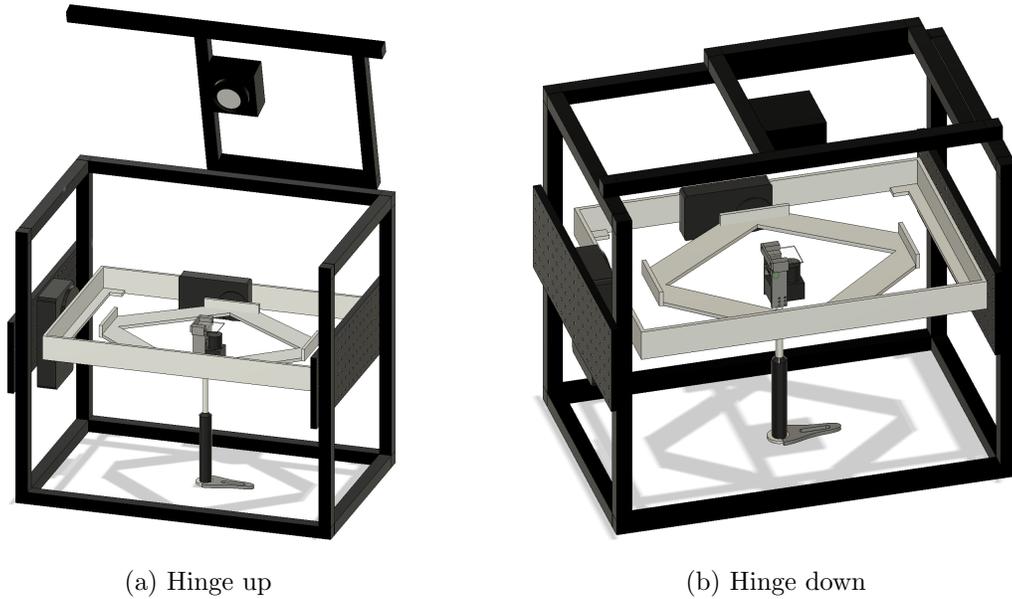
Figure 13: Angled views of the full apparatus with the hinged mirror mount in an open and closed position. All components are to scale.

A special fixture was designed to contain the optical test equipment and to provide a rotary mount to hold and move the test specimen. The inner diamond-shaped mount seen in Figure 13 was custom-fabricated from aluminum and lined with foam tape. This was then attached to a medium-load stage, which created an axis of rotation. These two components were then attached to a rectangular outer mount that was also custom-fabricated from aluminum. To create an orthogonal axis of rotation, the inner rotation system was attached to a high-load rotation stage. The outer mount and its associated rotation stage were secured to oversized breadboards on both ends to relieve cantilever stress. The breadboards were secured to an external frame that also featured a spherical mirror mounted on the top face. A hinge was included to simplify placing and removing any tested equipment into the inner mount.

To accomplish the moiré interferometry, custom aluminum brackets held together the optical system (shown in Figure 14). This consisted of an LED board whose emissions would pass through three squares of opal diffusing glass before intersecting the Ronchi ruling. This light then reflected from the spherical mirror and entered the camera's lens after a secondary pass through the Ronchi ruling. Both the brackets and camera were elevated to an optimized height with an optical post and post holder. This height will always be influenced by the focal length of the spherical mirror.

All of this was supported by a variety of components that are off-the-shelf with the exception of three portions. The first was the inner and outer visor mounts fabricated from aluminum. The second was the LED board, which was wired in lab.
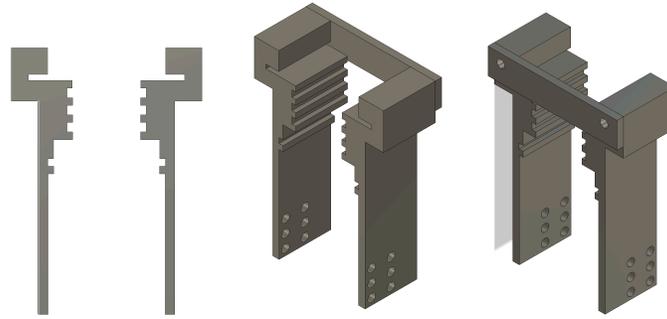
Figure 14: Drawing showing different views of the custom designed bracket for mounting the light source, opal glass, and Ronchi ruling to the camera.

(a) Optical

(b) Frame

(c) Rotations

(d) Mirror
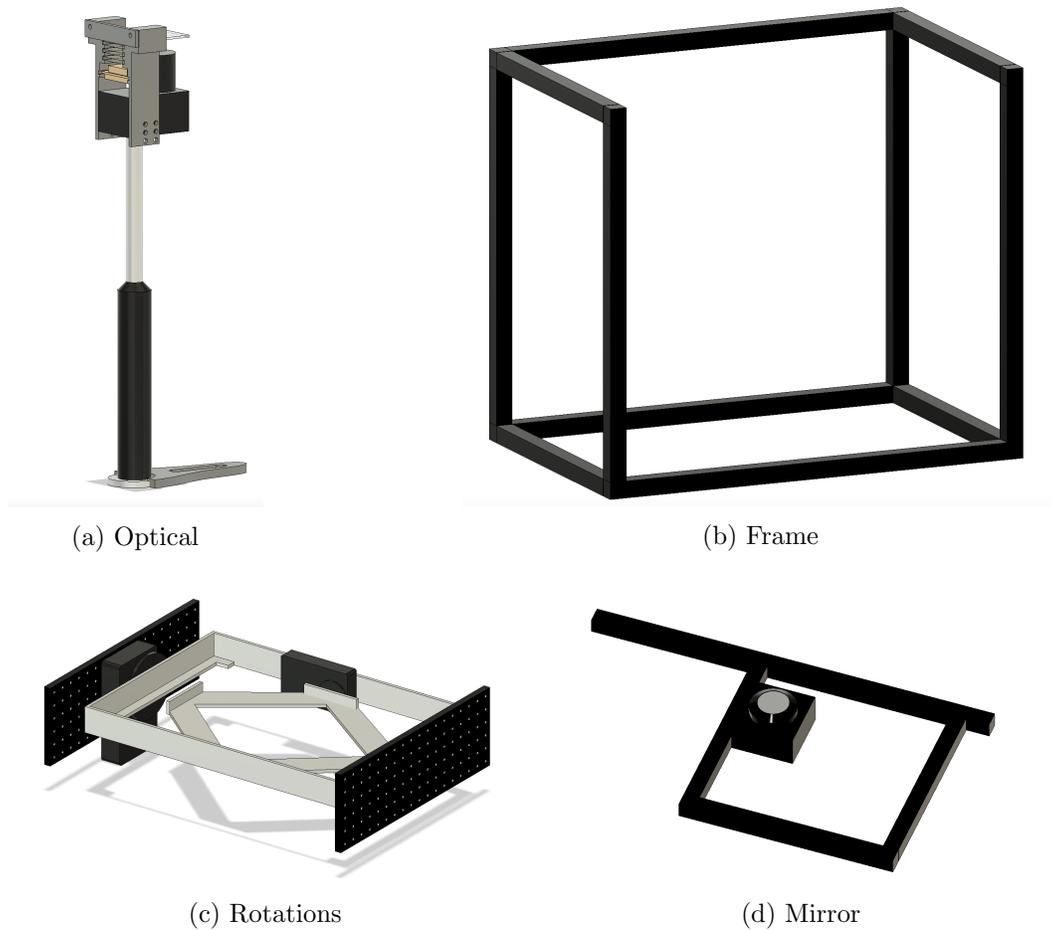
Figure 15: Broken-down sections of the apparatus in Figure 13 for ease of reference.

The third was a set of aluminum brackets that held together the Ronchi ruling, opal glass, camera, and LED board for the optical system. To aide in future replication, the parts seen in Figures 15a–15d are respectively listed in Tables 1–4. Smaller pieces of hardware that were critical but not rendered are found in Table 5.

Table 1: Equipment used to construct the optical system (Fig. 15a).

Section	Part Name	Distributor	Model	Quantity
Optical	25mm Fixed FL Lens	Edmund Optics	#59-871	1
Optical	PL-D Camera Mount	Edmund Optics	#89-407	1
Optical	PixeLink Camera	Edmund Optics	#89-398	1
Optical	Ronchi Ruling	Edmund Optics	#56-606	1
Optical	Opal Diffusing Glass	Edmund Optics	#46-167	3
Optical	6" Optical Post	Newport	SP-6	1
Optical	6" Post Holder	Newport	VPH-6-P	1
Optical	Clamping Fork	Newport	PS-F	1
Optical	Custom system holder	(manufactured on-center)		1
Optical	Custom LED board	(circuited in-lab)		1

Table 2: Equipment used to construct the framework of the apparatus (Fig. 15b).

Section	Part Name	Distributor	Model	Quantity
Frame	Quick Corner Cube	ThorLabs	XE25W3	8
Frame	Construction Rail, 15"	ThorLabs	XE25L15	4
Frame	Construction Rail, 24"	ThorLabs	XE25L24	3
Frame	Construction Rail, 21"	ThorLabs	XE25L21	4

Table 3: Equipment used to construct the rotary stages and visor cradle (Fig. 15c).

Section	Part Name	Distributor	Model	Quantity
Rotations	Breadboard, 6" x 18"	Thor Labs	MB618	2
Rotations	High-Load Stage	Zaber	X-RST-E Series	1
Rotations	Medium-Load Stage	Zaber	X-RSW-E Series	1
Rotations	Custom outer mount	(manufactured on-center)		1
Rotations	Custom inner mount	(manufactured on-center)		1

Table 4: Equipment used to construct the hinged mirror mount (Fig. 15d).

Section	Part Name	Distributor	Model	Quantity
Mirror	Construction Rail, 12"	ThorLabs	XE25L12	3
Mirror	Construction Rail, 24"	ThorLabs	XE25L24	1
Mirror	Quick Corner Cube	ThorLabs	XE25W3	4
Mirror	Spherical Mirror	Edmund Optics	#32-815	1
Mirror	Kinematic Mirror Mount	Edmund Optics	#53-964	1

Table 5: Hardware used in construction but not explicitly seen in renderings.

Section	Part Name	Distributor	Model
Not depicted	Slim Right-Angle Brackets	ThorLabs	AB90H
Not depicted	Tee Gusset Plate	ThorLabs	XE25GP2
Not depicted	Elbow Gusset Plate	ThorLabs	XE25GP2
Not depicted	1/4"-20 Channel Screw, 5/8"	ThorLabs	SH25LP63
Not depicted	1/4"-20 Channel Screw, 3/8"	ThorLabs	SH25LP38
Not depicted	Low-Profile T-Nut	ThorLabs	XE25T3
Not depicted	Drop-In T-Nut	ThorLabs	XE25T1
Not depicted	Hinge	ThorLabs	XE25H
Not depicted	Hair Pin Cotter	MSC	#51243327
Not depicted	Bronze Sleeve Bearing	MSC	#06454516
Not depicted	Standard Clevis Pin	MSC	#67932608

4   Modeling Software Design

4.1   Overview

The following novel model simulates imaging prior to experimentation to allow for optimization in both post-processing and designing the interferometric framework by accounting for lensing effects resulting from optical-paths incident to curved surfaces. Designed with modularity in mind, it can allow for future image coupling for objects of any material, shape, or size with infinitely possible spacing arrangements and equipment specifications.

It begins by defining mathematical representations for the curved visor as well as the moiré interferometry apparatus designed for the project. These parameters include: the geometric shape & size of the spherical mirror, Ronchi ruling, and object intended for inspection (visor); the material (index of refraction) of the visor; the orientation and positioning of the Ronchi ruling, camera, and spherical mirror; the camera's field-of-view and resolution; the axes of rotation for the visor mount; and the separation between each of the apparatus' components.

With this information, the model can accomplish two main tasks. The first and simplest is to calculate an optimized sequence of imaging such that the entire visor is captured with minimal overlap. This ordering of angular rotations necessary to achieve full coverage is output to a datafile (in a user specified format) along with a separate Mathematica notebook that contains a 3D graphic of the visor labeled with numbered subsections to allow for ease of reference after imaging. The second and more complex component simulates expected imaging results by coupling the three-dimensional vector form of Snell's Law and differential geometry as a ray tracer. It reverse-calculates the image pixel-by-pixel (or to a desired resolution) by determining the most likely path a light-source would travel as it initially passes through the Ronchi ruling, gets refracted based on the angle-of-incidence and material of the curved visor, reflects off the spherical mirror of a given focal length, is again refracted with a second pass-through of the curved visor, and then intersects

the Ronchi ruling for a final time.

Depending on the alignment of the Ronchi ruling intersections, a pixel-value with either be totally polarized (dark), partially polarized (gray), or unaffected (white). Unlike moiré interferometry for flat surfaces, the visor introduces inherent curvature to the resulting Ronchi lines, making this "ideal" simulated image valuable for post-imaging distortion detection.

4.2 Experiment Reproduction

Our first step was to be able to represent the curved surface and apparatus used for imaging as described in the Hardware section. The following subsections discuss the steps taken to model the respective components and curved surfaces.

4.2.1 xEMU Visor

(a) xEMU visor

(b) Modeled visor

Figure 16: Comparison between the real and mathematically modeled visors.

Most physical surfaces can be modeled using mathematical representations. For our case, we focused on modeling the Artemis xEMU helmet visor. Based upon the technical drawings, we were able to represent its general shape as an oblate spheroid, meaning that two of the semi-axes had equivalent magnitudes and the third semi-axis was smaller than the others:

$$\frac{x^2}{a^2} + \frac{y^2}{b^2} + \frac{z^2}{c^2} = 1 \longrightarrow \frac{(x - x_0)^2}{a^2} + \frac{(y - y_0)^2}{c^2} + \frac{(z - z_0)^2}{c^2} = 1 \qquad (27)$$

To model this in Mathematica, it becomes necessary to isolate the z-component such that it becomes a function of x and y that represents the top-half of an ellipsoid:

$$S(x, y) = z = z_0 + \sqrt{c^2 - \frac{c^2(x - x_0)^2}{a^2} - (y - y_0)^2} \qquad (28)$$

Equation (28) was then used to represent the inner and outer surfaces for both the inner pressure bubble and outer protective visor. Each visor was thus modeled as the upper portion of two concentric oblate spheroids with a material index of refraction matching polycarbonate ($n = 1.59$) between the two surfaces. A comparison between the physical visor imaged in the lab and the Mathematica representation is seen in Figure 16.

4.2.2 Ronchi Ruling

The Ronchi ruling was represented by a plane bounded by four corners to mimic the 2×2 inch square. It is centered in the xy-plane parallel to the axes of rotations in neutral position, with a height determined by the extensions of the optical post. Rectangular regions subdivide the bounded plane to represent the clear and dark line pairs. Figure 17 compares a sample of 25 line pairs per inch Ronchi rulings against the models' rendition. Note that in Figures 17b and 17c, every other rectangular subdivision is plotted to visually represent the clear and dark lines.
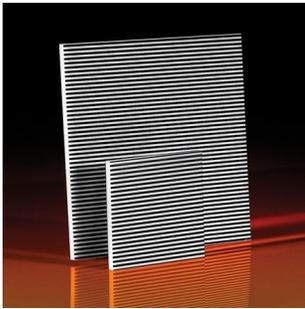
(a) Edmund Optics #59-518 25 lpi Ronchi ruling
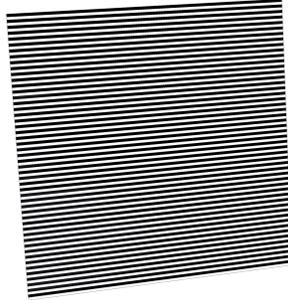
(b) Modeled Ronchi ruling, tilted to resemble image
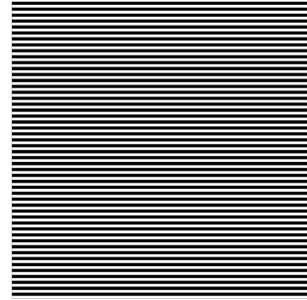
(c) Modeled Ronchi ruling, orthogonal view

Figure 17: Comparison between the real and mathematically modeled Ronchi rulings.

4.2.3 Camera

One of the main issues to resolve was determining the camera's field of view. We began by looking at the lens' documentation and determined the effective focal length (EFL) to be 25 mm. Next, we looked into the camera's documentation to determine the pixel pitch size and the number of horizontal and vertical pixels. The pitch size was provided as 1.4 μm and the resolution was 4608×3288 pixels. Then we used the equation relating these three values to the horizontal and vertical field of view:

$$FOV_{\leftrightarrow} = 2\tan^{-1}\left(\frac{\text{width}}{2 \times \text{EFL}}\right) = 2\tan^{-1}\left(\frac{4608\,\text{pixels} \times 0.0014\frac{\text{mm}}{\text{pixel}}}{2 \times 25\,\text{mm}}\right) = 14.7°$$

$$FOV_{\updownarrow} = 2\tan^{-1}\left(\frac{\text{height}}{2 \times \text{EFL}}\right) = 2\tan^{-1}\left(\frac{3288\,\text{pixels} \times 0.0014\frac{\text{mm}}{\text{pixel}}}{2 \times 25\,\text{mm}}\right) = 10.5°$$

In addition to the field of view, we determined the camera's imaging point based on the number of Ronchi ruling lines in view through imaging and the physical separation between the camera lens and the Ronchi ruling. It is from this imaging point that a field-of-view originates its span.

4.2.4 Spherical Mirror

The spherical mirror was modeled as a sphere with a radius that was twice the mirror's focal length, i.e. it's radius of curvature. The region of visibility was taken to be a radial distance of half the mirror's diameter from the physical mirror's center. For our case, we used a 2-inch spherical mirror with a focal length of 4 inches placed about 7.5 inches above the Ronchi ruling. In addition to denoting where the mirror's physical center was located, the theoretical center of the spherical mirror's radii of curvature was calculated to be between the light source and the camera's imaging point. This matched the expected alignment through the physical tip and tilt from the mirror's mount.

4.2.5 Mounts and Stages

While not visually depicted in the model, the inner and outer mounts are within the same planes as the axes of rotations and determine the initial height of the curved surface. They are attached to the rotary stages and are therefore critical in the proceeding calculations. The inner mount holds the visor and is associated with an independent axis of rotation, R_x. The outer mount holds the inner mount, and is therefore considered a dependent axis of rotation, R_y. We denote the intersection of these rotational axes as $(x, y, z) = (0, 0, 0)$, and represent the locations of the previous components with respect to their separation from this origin.

4.3 Rotations

Since rotating a surface is more complicated than applying rotations to coordinate values, we maintained the visor as a stationary reference frame and instead represented the inner and outer mount rotations as applied to the other apparatus components. As mentioned in the previous section, the apparatus consisted of two rotary stages and consequently two axes of rotation: R_x and R_y. Triggering a rotation of $\Delta\theta$ for the inner mount results in the operative application of the following transformation:

$$R_x = \begin{bmatrix} 1 & 0 & 0 \\ 0 & \cos(\Delta\theta) & \sin(\Delta\theta) \\ 0 & -\sin(\Delta\theta) & \cos(\Delta\theta) \end{bmatrix} \tag{29}$$

Triggering a rotation for the outer mount is more complex as a result of its dependency on the inner mounts rotation. While this complicates the rotation matrix, it does guarantee commutation between R_x and R_y, which simplifies calculations later on. We thus consider a unit vector to represent the y-axis in a neutral position as $\vec{u} = \langle 0, 1, 0 \rangle$. It is updated following any inner mount rotation $\vec{u}' = R_x\vec{u}$, and maintains its orthonormality such that $u'^2_x + u'^2_y + u'^2_z = u^2_x + u^2_y + u^2_z = 1$ for any and all subsequent rotations. It then follows that an outer mount rotation of $\Delta\phi$ is represented by a rotation matrix of:

$$R_y(\vec{u}) = \begin{bmatrix} \cos\Delta\phi + u_x^2\left(1 - \cos\Delta\phi\right) & u_x u_y\left(1 - \cos\Delta\phi\right) + u_z\sin\Delta\phi & u_x u_z\left(1 - \cos\Delta\phi\right) - u_y\sin\Delta\phi \\ u_y u_x\left(1 - \cos\Delta\phi\right) - u_z\sin\Delta\phi & \cos\Delta\phi + u_y^2\left(1 - \cos\Delta\phi\right) & u_y u_z\left(1 - \cos\Delta\phi\right) + u_x\sin\Delta\phi \\ u_z u_x\left(1 - \cos\Delta\phi\right) + u_y\sin\Delta\phi & u_z u_y\left(1 - \cos\Delta\phi\right) - u_x\sin\Delta\phi & \cos\Delta\phi + u_z^2\left(1 - \cos\Delta\phi\right) \end{bmatrix}$$

$$(30)$$

In summary, a coordinate position represented as vector $\vec{x}$ would be transformed by two means. The first is an inner mount rotation followed by an outer mount rotation:

$$\vec{x}' = R_y(\vec{u}')R_x\vec{x}$$

The second is an outer mount rotation followed by an inner mount rotation:

$$\vec{x}' = R_x R_y(\vec{u})\vec{x}$$

...where again, the commutative nature of the coupled axes of rotations implies:

$$\vec{x}' = R_y(\vec{u}')R_x\vec{x} = R_x R_y(\vec{u})\vec{x}$$

This procedure is applied to all coordinate representations within the system. For intersections of planes, such as those to be discussed in the following section, the coordinates undergo the respective transformation, and their distance between the imaging point becomes a vector. This vector is then used to calculate the updated intersection.

4.4 Determining View Area

While the rotation stages are in a neutral position, the initial incident viewing area is found by projecting sloped planes representing the camera's field-of-view and determining their intersection with the curved surface. These planes all intersect at the camera's imaging point, $(x_{cam}, y_{cam}, z_{cam})$. For the horizontal span, $FOV_{\leftrightarrow}$, the camera's field-of-view planes are represented by z_x:

$$z_x\left(x, x_{cam}, z_{cam}, \theta\right) = \cot\theta \cdot \left(x - x_{cam}\right) + z_{cam} \tag{31}$$

...where $\theta \in \left[-\frac{FOV_{\leftrightarrow}}{2}, \frac{FOV_{\leftrightarrow}}{2}\right]$. On the other hand, the vertical span, $FOV_{\updownarrow}$, is represented by sloped planes z_y:

$$z_y\left(y, y_{cam}, z_{cam}, \phi\right) = \cot\theta \cdot \left(y - y_{cam}\right) + z_{cam} \tag{32}$$

...where $\phi \in \left[-\frac{FOV_{\updownarrow}}{2}, \frac{FOV_{\updownarrow}}{2}\right]$. Once the equations are reduced to a single variable function of x or y, they can be used to find the intersections between the camera's field-of-view and the curved surface. This is accomplished by determining the x, y, and z values such that Equation (33) holds:

$$z_x\left(x_i, x_{cam}, z_{cam}, \theta\right) = z_y\left(y_j, x_{cam}, z_{cam}, \phi\right) = S(x_i, y_j) \tag{33}$$

...where $S(x_i, y_j)$ is some z-coordinate dependent on x_i and y_j on the curved surface. Naturally, the values of x_i and y_j will subsequently be dependent on the angles θ
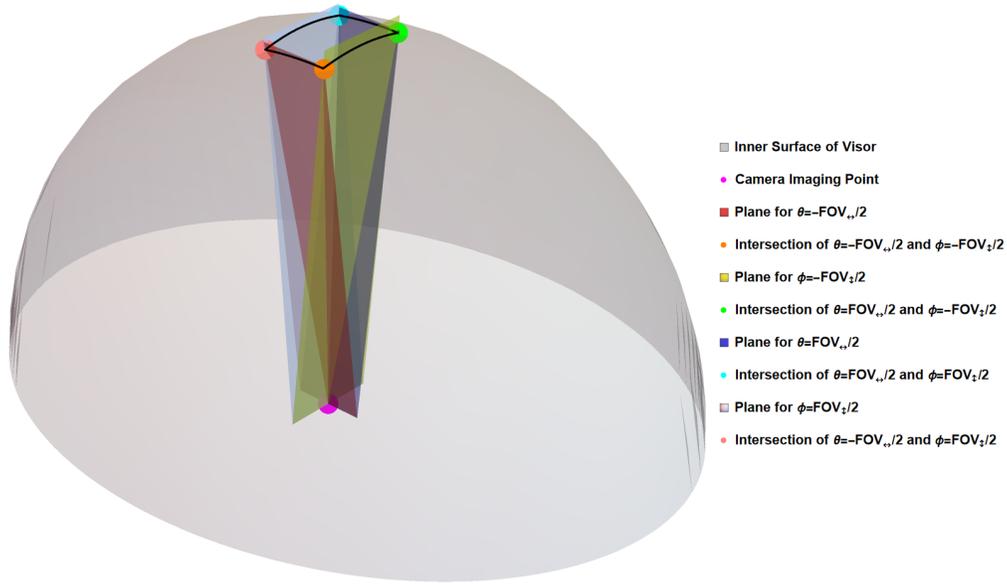
Figure 18: Incident-camera view for neutral position (no mount rotations).

and ϕ. When the boundary cases of z_x and z_y are plotted, i.e. at $\theta = \pm\frac{FOV_{\leftrightarrow}}{2}$ and $\phi = \pm\frac{FOV_{\updownarrow}}{2}$, the camera's view area of the visor becomes clearer to understand. These plane and surface intersections are depicted in Figure 18.

As a result of the multi-variable dependence for Equations (31) and (32), they can be applied to any curved surface for any camera position and field-of-view. Figures 19a – 19f compare two example surfaces with differing camera positions and field-of-views. It is important to note that these equations only hold when the mount is in neutral position. As such, the script only calculates based on Equations (31), (32), and (33) for the initial set of coordinates before switching methods to determine the camera's view area following a rotation.

Once a rotation or rotations have been applied, the method mentioned in the Rotations section becomes dominant. Consider an intersecting coordinate $C = (x, y, z)$ that has undergone a set of rotations to become $C' = (x', y', z')$. This coordinate is not guaranteed to perfectly intersect the curved surface, and as such a parametric method is introduced. The vector between the initial imaging point $P = (x_{cam}, y_{cam}, z_{cam})$ and the initial intersection coordinate is $C - P$. To determine when this intersects with the curved surface, we introduce the parametric variable s and define:

$$\vec{C} = (C - P)s + P = \begin{bmatrix} (x - x_{cam})s + x_{cam} \\ (y - y_{cam})s + y_{cam} \\ (z - z_{cam})s + z_{cam} \end{bmatrix}$$

...making note that for the stationary case, the solution is $s = 1$. This vector undergoes the set of rotations performed by the rotation stages, say $R_x R_y(\vec{u})$, and

(a) $FOV_{\leftrightarrow} = 27°, FOV_{\updownarrow} = 32°$, angled view

(b) $FOV_{\leftrightarrow} = 22°, FOV_{\updownarrow} = 22°$, angled view

(c) $FOV_{\leftrightarrow} = 27°, FOV_{\updownarrow} = 32°$, top view

(d) $FOV_{\leftrightarrow} = 22°, FOV_{\updownarrow} = 22°$, top view

(e) $FOV_{\leftrightarrow} = 27°, FOV_{\updownarrow} = 32°$, side view

(f) $FOV_{\leftrightarrow} = 22°, FOV_{\updownarrow} = 22°$, side view
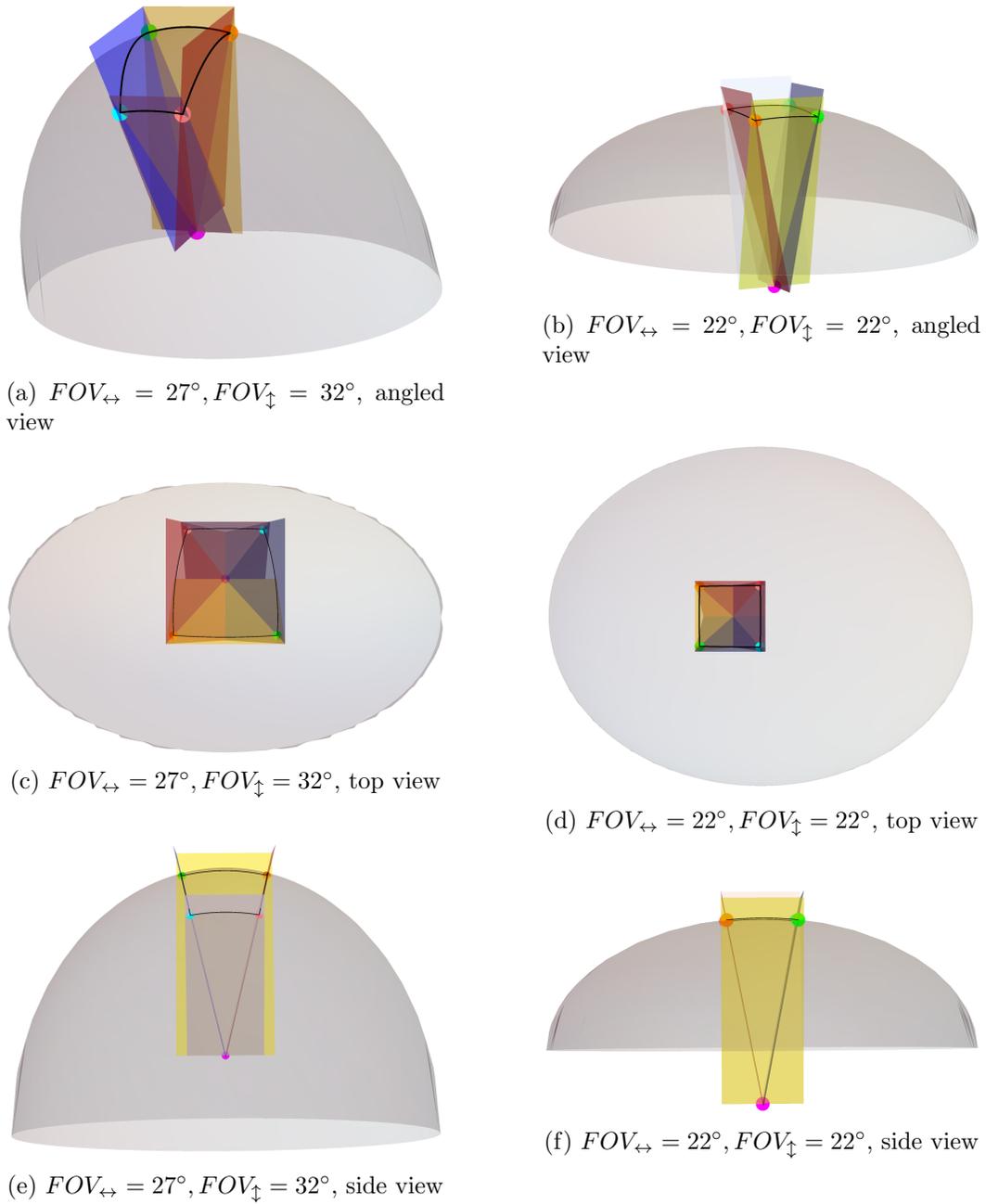
Figure 19: Sample incident-camera views for various arrangements in neutral position (no mount rotations).

becomes:

$$\vec{C}' = R_x R_y(\vec{u})\vec{C} = \begin{bmatrix} x'(s) \\ y'(s) \\ z'(s) \end{bmatrix}$$

...where the transformed x, y, and z coordinates are a function of the parametric

variable s. The next step is to solve the following equality for s, again recalling the curved surface equation $S(x, y)$:

$$S\left(x'(s), y'(s)\right) = z'(s) \tag{34}$$

Once the value for s has been determined, it is substituted back into $\vec{C}'$ and reduced to the transformed intersection coordinate C'. This process is performed for all denoted coordinates.

A benefit of including these calculations can allow the user to pre-determine the set of rotations required to image the surface. There is a portion of the script dedicated to outputting the logical ordering of mount rotations and it includes a visualization of the location for each resulting image. It considers any apparatus or rotation based limitations. Finally, it also allows for clear identification of problem areas that do not reach the criteria for acceptability post-processing. Figure 20 shows the result for a camera with a square cropped field-of-view that required 179 images to cover the surface.


(a) Front view   (b) Back view
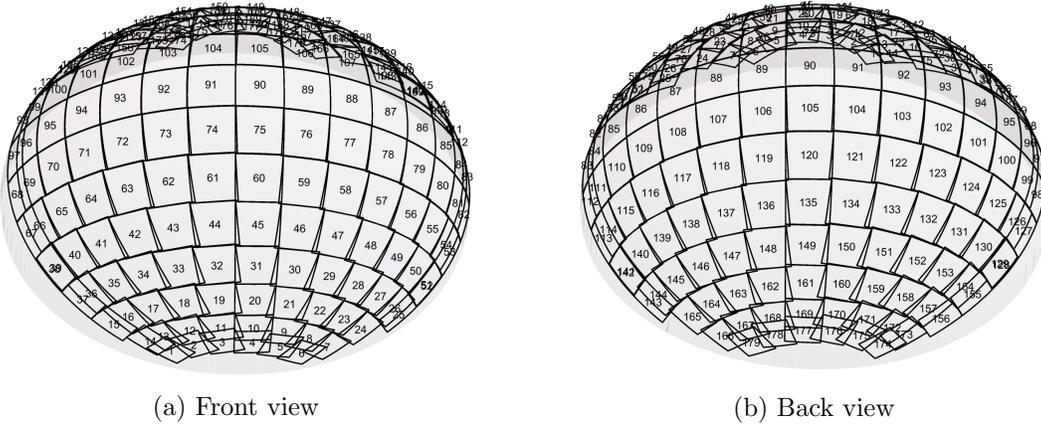
Figure 20: Front and back view of ordered images to capture the surface.

4.5 Simulated Ray Tracing

The developed algorithm uses an inverse process that begins at the center of a theoretical camera pixel and reverses through the most likely path towards the light source. The positions of intersection with the Ronchi ruling along this path determines whether the pixel will register as fully or partially polarized, or completely unaffected. This portion of the script is designed to run parallelized, so the focus will be on explaining and visualizing the mathematics for any single ray path.

4.5.1 Normalized Surface Equations

The normal vector for a surface is perpendicular to the tangent plane at any point on the surface. For curved surfaces, this normal changes depending on the position of observation. To properly simulate a ray-tracing, these normals will need to be calculated for both the curved surface of inspection and the spherical mirror. We will

26

begin by focusing on the general formula for a normal surface before extrapolating to its applications.

Consider a surface $S(x, y)$ in three-dimensional space. The normal equation for a point (x_i, y_i, z_i) on the surface will depend on which side of the surface the incoming ray intersects. Generally, the surface normal is in opposition to the direction of an incoming ray. Thus, for a ray $\vec{r} \to z = z_i^-$, i.e. traveling in an outwards direction with respect to the origin, the normal equation is:

$$\vec{N}_i^- = \left\langle \frac{\partial S}{\partial x}\bigg|_{x_i, y_i}, \frac{\partial S}{\partial y}\bigg|_{x_i, y_i}, -1 \right\rangle \tag{35}$$

Contrapositively, for a ray $\vec{r} \to z = z_i^+$, i.e. traveling in an inwards direction towards the origin, the normal equation is instead:

$$\vec{N}_i^+ = \left\langle -\frac{\partial S}{\partial x}\bigg|_{x_i, y_i}, -\frac{\partial S}{\partial y}\bigg|_{x_i, y_i}, 1 \right\rangle \tag{36}$$

For both Equation (35) and (36), their unit normal is calculated as follow:

$$\hat{N}_i = \frac{\vec{N}_i}{\sqrt{\left(\frac{\partial S}{\partial x}\bigg|_{x_i, y_i}\right)^2 + \left(\frac{\partial S}{\partial y}\bigg|_{x_i, y_i}\right)^2 + 1}} \tag{37}$$

4.5.2 Three-Dimensional Reflections

The first application to discuss regards the reflection of an incident ray $\vec{r}_{in} \to \vec{r}_{re}$ after hitting the spherical mirror. The result of an incident ray $\vec{r}_{in}$ hitting the mirror at a point $(x_{mirror}, y_{mirror}, z_{mirror})$ with normal surface $\hat{N}_{mirror}$ is defined as:

$$\vec{r}_{re} = \vec{r}_{in} - 2\left(\vec{r}_{in} \cdot \hat{N}_{mirror}\right)\hat{N}_{mirror} \tag{38}$$

This of course assumes perfect reflection, which is not guaranteed for most coatings on spherical mirrors. Nonetheless, it is a reasonable assumption for the practicality of the model.

4.5.3 The Visor-less Case

Figure 21 details a theoretical ray-tracing when just the optical system and mirror mount are in place.

4.5.4 Three-Dimensional Snell's Law

Consider an incoming ray originating at point (x_0, y_0, z_0), where the index of refraction is n_1, that becomes incident on a material with index of refraction n_2 and normal surface $\hat{N}_i$ at intersection point (x_i, y_i, z_i). Its normalized incident path is

■ Spherical Mirror

☐ Ronchi Ruling Visual

● Spherical Mirror RoC

— Normal 2 Mirror Intersect

● Camera Location

● Intersection of Camera's Center View Directly to Ronchi Ruling

— Camera View (air medium)

● Intersection of Ray to Mirror without a Visor

— Test Reflected Ray

● Intersection of Center View to Ronchi Ruling without Visor Lensing
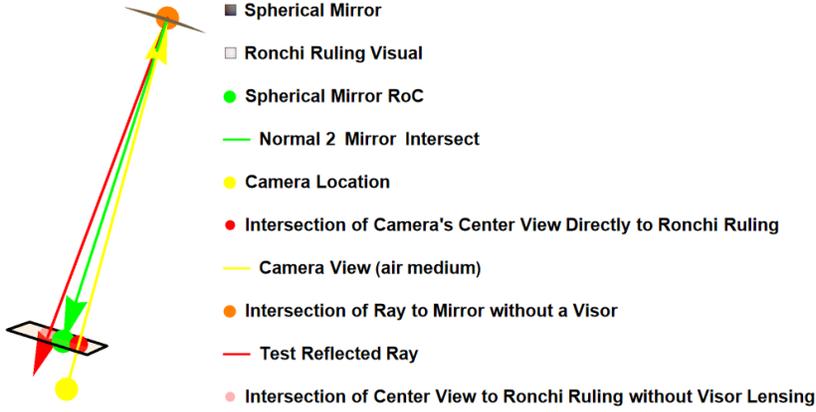
Figure 21: Macro-view of ray reflection without a visor in place.

defined as $\hat{r}_{in} = \frac{\vec{r}_{in}}{|\vec{r}_{in}|}$, where $\vec{r}_{in} = \langle x_i - x_0, y_i - y_0, z_i - z_0 \rangle$, and the refracted ray through the material with index of refraction n_2 is defined as:

$$\hat{r}_{out} = \frac{n_1}{n_2} \hat{N}_i \times \left(-\hat{N}_i \times \hat{r}_{in} \right) - \hat{N}_i \sqrt{1 - \frac{n_1^2}{n_2^2} \left(\left(\hat{N}_i \times \hat{r}_{in} \right) \cdot \left(\hat{N}_i \times \hat{r}_{in} \right) \right)} \qquad (39)$$

...which is a 3D form of *Snell's Law*, and it allows us to follow a propagated light path through materials with different indices of refraction. More importantly, we are able to accurately consider any inherent lensing effects resulting from the surface's curvature.

It is important to note the limitations of the script with respect to its use of Equation (39). The script neglects any coatings or films on the visor. In the future it can be altered to include additional transitions between materials, but for now it is limited to a single change in material.

4.5.5 The Visor Case

The following depiction mimics the full apparatus in operation. Consider that an incoming ray $\vec{r}_{in,1}$ is incident on the visor at a point (x_1, y_1, z_1) with a normal surface $\vec{N}_1$. It is then refracted as it passes into the visor, $\vec{r}_{out,1} = \vec{r}_{in,2}$. The refracted ray then passes through the visor until it reaches air at a point (x_2, y_2, z_2) with a normal surface $\vec{N}_2$. It is again refracted when it exits the visor $\vec{r}_{out,2} = \vec{r}_{in,3}$.

The ray subsequently interacts with the spherical mirror, which has a normal surface $\hat{N}_{mirror}$ at the point of intersection $(x_{mirror}, y_{mirror}, z_{mirror})$, and is reflected: $\vec{r}_{re} = \vec{r}_{in,4}$. It continues propagating until it reaches the visor for a second time, and follows the same pattern until it exits the visors material near the optical system. In all, the ray has been refracted four times and reflected once.

The spacing in Figure 22 makes it difficult to distinguish each of the items on the legend, so we will demonstrate the localized ray tracings for the initial and secondary passes through the visor in Figure 23.
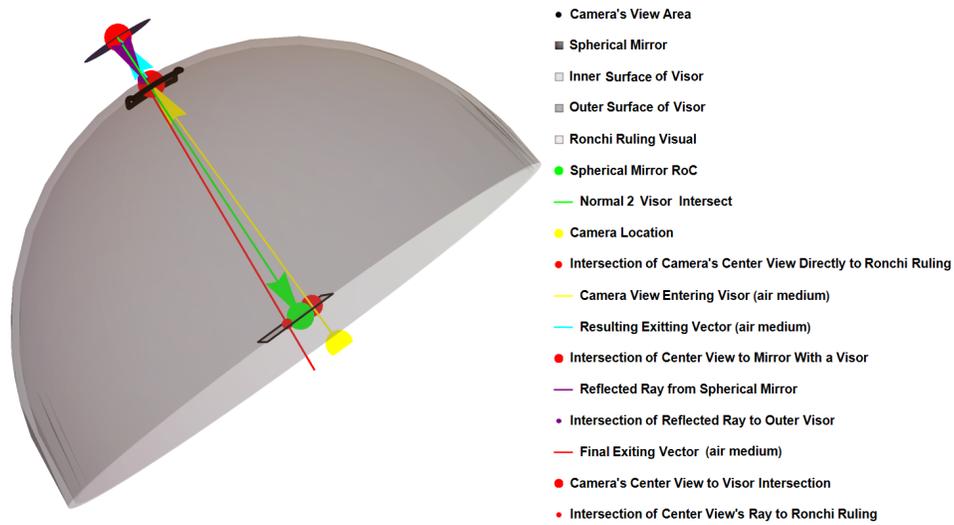
Figure 22: Macro-view of ray tracing with the visor in place.
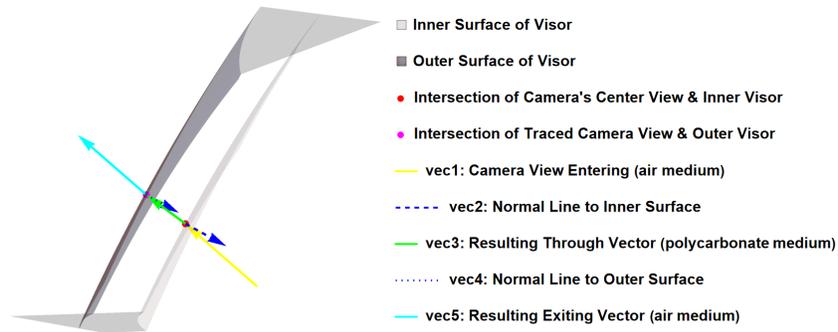
(a) Initial pass through the visor, depicts Eq. (35)
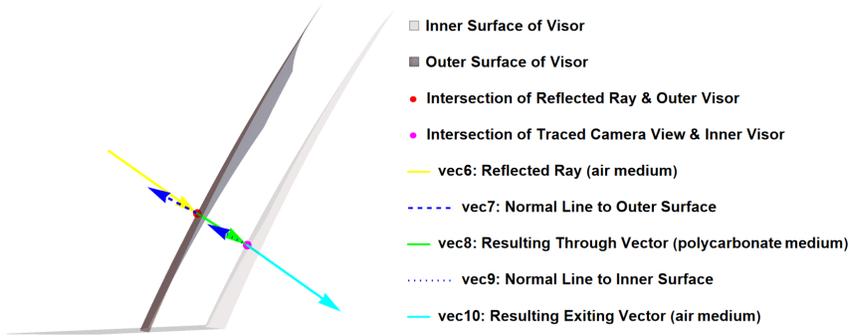
(b) Secondary pass through the visor, depicts Eq. (36)

Figure 23: Plots of the localized ray tracing through the visor.

4.5.6 Simulation Results

The result for running the entire ray-tracing algorithm to simulate the expected image for a visor-free case is seen in Figure 24. The high-resolution image taken of

(a) Real 4608 × 3288 pixel image　　　(b) Simulated 1106 × 789 pixel image
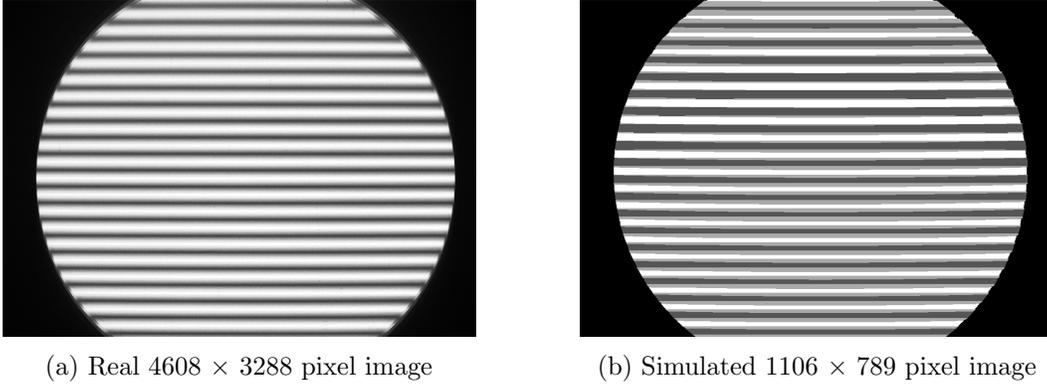
Figure 24: Comparison of the real (desaturated) reference image and the model simulation image with the consideration of the apparatus' arrangement and spacings.

the physical system in Figure 24a is significantly blurrier than the simulated image. As evidenced in Figure 24b, perfectly aligning the model to the physical system is equally as difficult as perfectly aligning the Ronchi ruling lines with a kinematic mount.

It is beneficial to compare the simulation results when there is and is not a visor in the system. Although there is not a noticable difference at-face between Figures 25a and 25b, the lensing effects are clearly pronounced in Figure 25c.


(a) Visorless Case　　　　　(b) Visor Case　　　　　(c) Difference
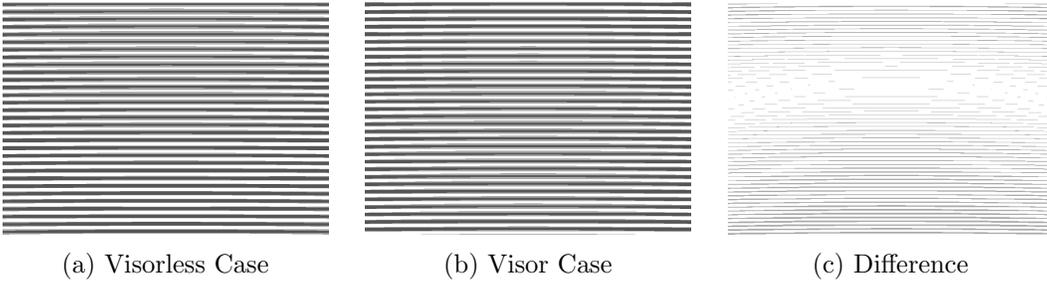
Figure 25: Comparison between the simulated moiré patterns when a curved visor is embedded into the system. Image resolutions are 758 × 541 pixels.

Beyond just general pattern prediction, the model can be used to determine the effect introducing an imperfection to the visor would create. In addition to the standard ellipsoidal equation mentioned above, a Gaussian bump on the order of $\exp(-\frac{(x^2+y^2)}{\sigma^2})$ was included as a term for the visor's outer surface equation. The results for an exceptionally aligned, low-resolution simulation are seen in Figure 26.

4.6　Benefits vs. Disadvantages

On the scale of simulating equally high resolution images, the computational cost is unfortunately too high to justify more than a few test cases. In the future, this may

| (a) Visorless Case | (b) Visor Case | (c) Difference |
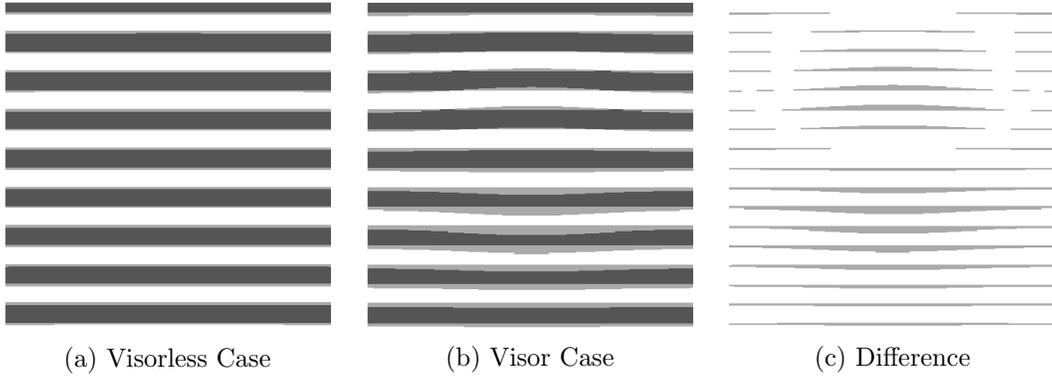
Figure 26: Comparison between the simulated moiré patterns when a Gaussian bump appears on the outer surface. Image resolutions are 440×440 pixels.

change if it gets translated into a lower-level language, possibly reducing the processing time. The model is however helpful when designing the system and preparing for testing. It inherently calculates spacing and directionality for aspects of the system, thus predicting advantageous combinations of spherical mirrors and component orientations. Since it is capable of determining the span of the surface to-be-imaged, it optimizing the number of images taken with minimal overlap without missing any regions. Similar to the program's accuracy by design, moiré interferometry has outstanding precision, but may exceed realistic requirements for everyday use.

5   Data Acquisition Software Design

The Zaber rotary stages used for each axis of rotation are controlled via National Instruments LabVIEW sample code that was provided by the vendor and then slightly modified to allow for movement in degrees. The LabVIEW sample code that served as a basis for this is called "Zaber A Series Control Panel.v". This software provides manual control for the stage allowing the user to command each stage individually to move to a given location by specifying the desired axis and the degrees of absolute or relative rotation. There is also a sensor that provides feedback of the absolute location of the rotary stage being commanded. While this software is useful for prototyping and troubleshooting, it becomes time consuming to use when needing to switch between many different locations.

Similarly, the camera vendor, Pixelink, provides free software to configure the camera and capture video or individual images. This is also useful for prototyping and troubleshooting but is limited as it doesn't interact with the rotary stage software. As a result, a custom program was written in LabVIEW using the Zaber software as a subVI. An Excel spreadsheet was used to create a coordinate list that was then used as an input for the LabVIEW code to facilitate a batch process. The code moves the stages sequentially to each location and captures a high resolution jpeg image. This proceeds until entire visor imagery is completed for one orientation of the Ronchi ruling. Each image is labeled and timestamped in the sequence it was captured. As discussed in other sections, the Ronchi ruling must be rotated

31

90 degrees to capture the distortion in the orthogonal direction to fully characterize each region. So, the program must be run a second time over the same coordinates to capture all of the imagery needed for the visor analysis.

6 Analysis Software Design

The distortion can be found by examining the image of the Ronchi ruling without the visor and determining the spacing between the edges of the lines and comparing it to the spacing in an image taken with the visor in place as discussed in Section 2 of this TM. This section will provide details on the image processing routines needed to perform these computations.

The first step in data processing is to read in a set of images captured with the camera: The two reference images with no visor present as shown in Figure 4 are used to compute the reference line spacing in the two Ronchi ruling orientations and the noise floor of the system. Pairs of images from the test article may then be read that correspond to the same location on the visor but with the Ronchi ruling rotated by 90 degrees in each image. After import the image is adjusted to improve contrast and cropped to center the circular region seen in the mirror. The image is then converted to grayscale, put through an averaging filter, an edge detector, and cropped to a 2800×2800 pixel square. The result is a series of lines one pixel wide. The first imported image is shown in Figure 27 along with the negative of the resulting square to better highlight the edges.

(a) import and first crop   (b) after edge detection
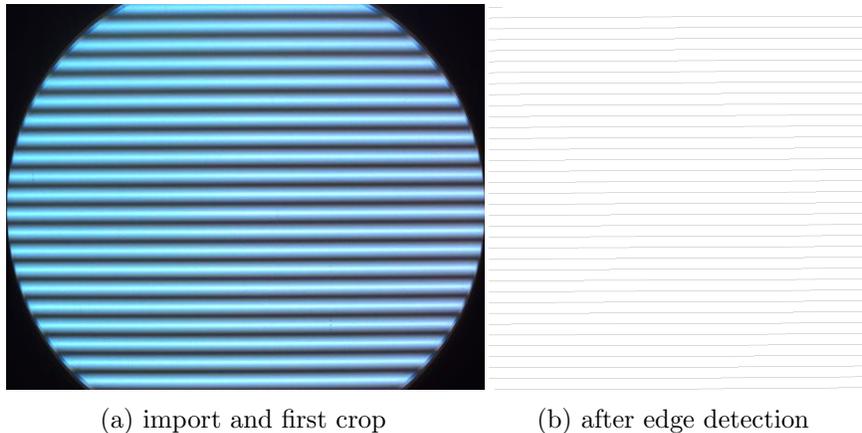
Figure 27: Images showing the results from the first two processing steps for the horizontal ruling image with no visor. Note that the lines on the right hand side are only a pixel wide and as a result are only faintly visible in this inverted image.

At this point the data is still in an image format. So, the next step is to convert it to a two dimensional array of zeros and ones, where the ones represent the lines. Next, the code determines the position of the ones in the array. This is then used to compute the average line spacing for the two images without the visor present. The position information is then used to compute the derivatives and scale them correctly to obtain distortion in the proper units. There are occasionally a few stray

pixels due to dust on the visor or a line that disappears along an edge. Both of these can result in a spike or skewing of the data. As a result, an averaging routine is used to average the distortion within a line spacing distance from the point. This has the effect of smoothing the data and removing most of the erroneous spikes as can be seen in a comparison between the before and after averaging plots shown in Figure 28.
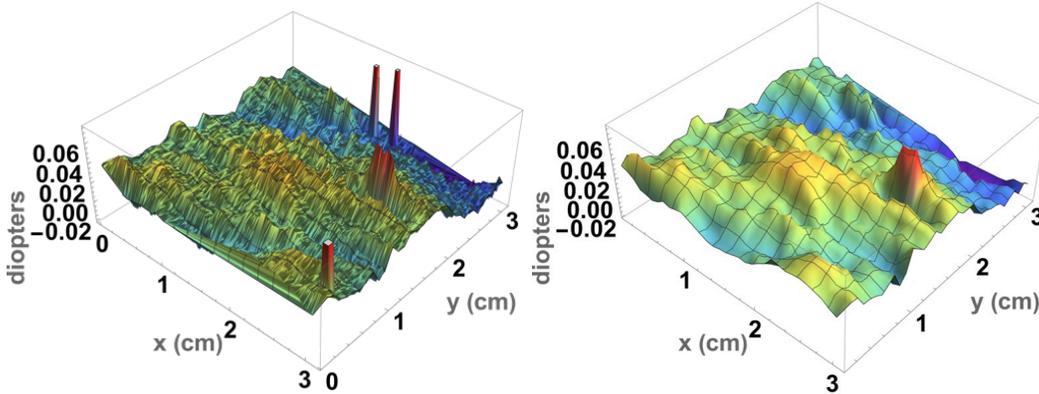

Figure 28: Images showing the results of the distortion computation before and after averaging

Figure 29 below shows the section of the photographs cropped out for processing and the processed images for the resulting Ronchi ruling images captured with the system. Please note that a 2800×2800 square pixel region is cropped from the center of the circular region in the photos for processing to make processing consistent and allow for the edges of the scan coordinates to better line up. The coordinate origin for this square in the photos is in the upper left with the x-axis aligning horizontally and the y-axis vertically. The RMS value of the noise for the two images is around 0.0019 diopters, but this will vary slightly depending on the image cropping done on the circular mirror image prior to processing.

Using the software to process the images in Figure 8, we see as in the Example subsection above that the average distortion is about 0.11 diopters but there is a large variation of ±0.1 diopters around that point due to the distortion in the center. The imagery is repeated in Figure 30 along with processed distortion plot for each.

7   Final Remarks and Future Extensions

An optical measurement system was designed, modeled, constructed, and tested for characterizing the distortion in curved optical surfaces. The noise floor was obtained by fitting a plane to the distortion plots for both the Ronchi ruling images with no sample present and then computing the square root of the sum of the squares of the differences between the data set and the fitted plane. This value will vary some depending on the image cropping that is performed but is approximately 0.002 diopters in magnitude. This is over 60 times less than the desired 0.125 diopter
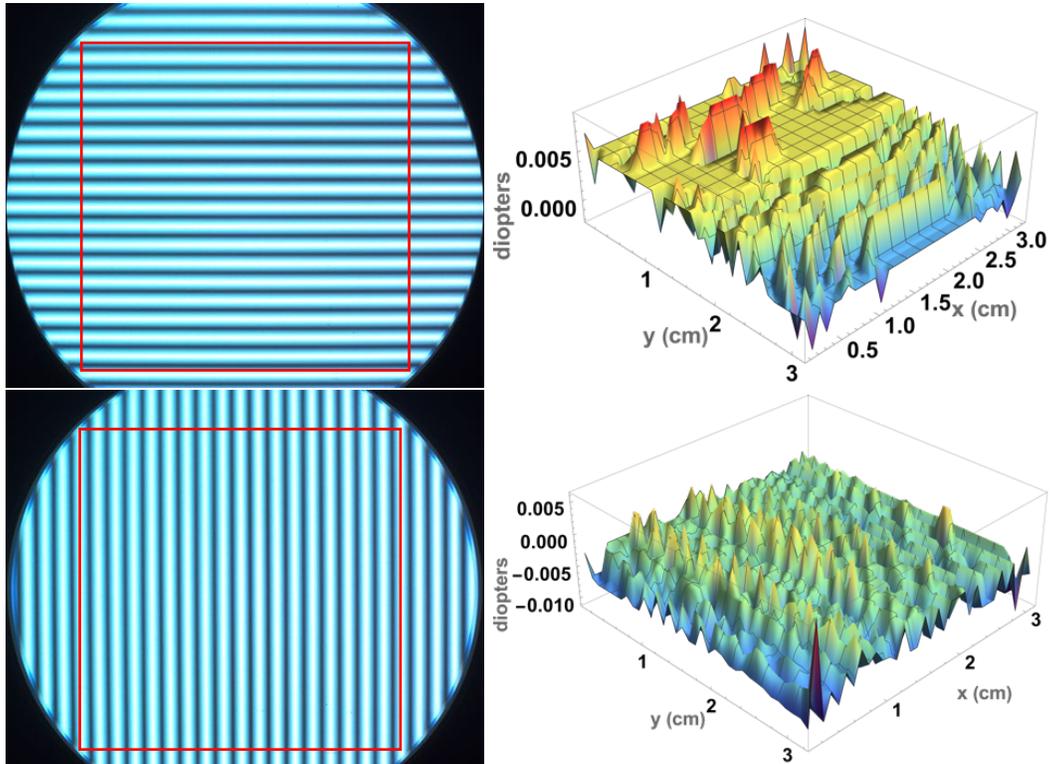
Figure 29: The top left photo shows the horizontal line pattern seen in the mirror with no sample present and the area that is cropped for processing. The coordinate system in the images has its origin in the upper left hand corner of the square with the +x axis extending to the right and the +y toward the bottom. The figure on the top right shows the processed image representing the noise floor. The bottom left and right figures are similar but for the vertical line pattern (Ronchi ruling rotated 90 degrees).
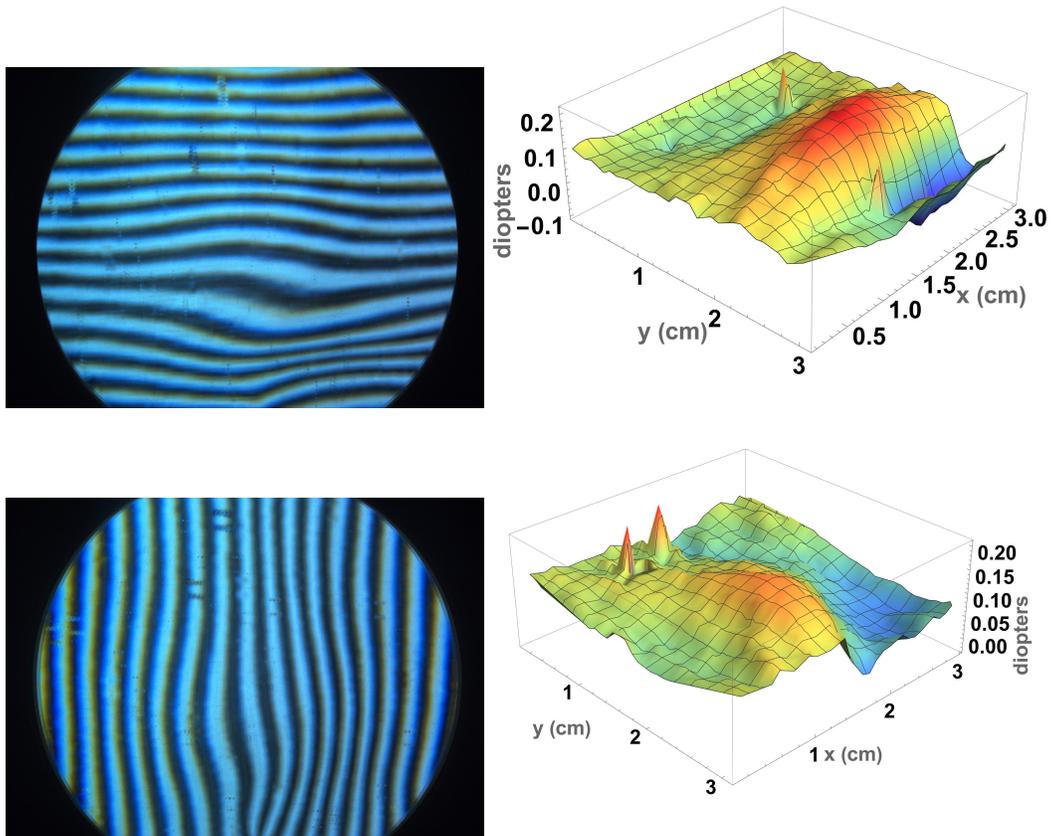
Figure 30: The top left photo shows the horizontal line pattern seen for an area with distortion present. The coordinate system in the images has its origin in the upper left hand corner of the square with the +x axis extending to the right and the +y toward the bottom. The figure on the top right shows the plot of the distortion computed for the processed image. The bottom left and right figures are similar but for the vertical line pattern (Ronchi ruling rotated 90 degrees). This shows that the coded algorithm is in agreement with the Example subsection above. The plots show an average offset of around 0.11 diopters with a variation of around ±0.1 diopters around that average. The small spikes are likely due to dust particles or small inclusions that block the light path.

detection limit and 6 times better than the targeted turn down ratio. The prior method using image comparison had a noise floor of about 0.05 diopters.

One important advantage of the new approach is that there are several degrees of freedom in placement of the key optical components with respect to the sample under test which allow you to reduce the sensitivity of the primary curvature of the sample while making the distortion more visible. Likewise, the distortion sensitivity may also be controlled by moving the Ronchi ruling toward or away from the focal point of the mirror. A small disadvantage of the approach is that the mirror causes the light to pass through the sample twice inspecting slightly different areas on each pass. This results in a double image of small inclusions and defects. However, this effect can be minimized by keeping the sample as close to the mirror as possible.

The system was recently used to test several production parts of the Artemis helmet, the pressure bubble, and the protective visor. Variations in the base material and coatings proved to be visible with the system and current plans include testing samples from future production runs. Additionally, at least one commercial company is considering using large curved windows in a future spacecraft where a system like this might be used in testing flight windows prior to assembly.

References

1. Youngquist, R. C., Nurge, M. A., and Skow, M., "A Comparison of Three Optical Methods for Measuring Distortion in Optical Windows," NASA/TM 2015-218822, Apr. 2015.

2. ASTM Standard F2156-17, 2017, "Standard Test Method for Measuring Optical Distortion in Transparent Parts Using Grid Line Slope," ASTM International, DOI:10.1520/F2156-17.

REPORT DOCUMENTATION PAGE		*Form Approved* *OMB No. 0704–0188*

The public reporting burden for this collection of information is estimated to average 1 hour per response, including the time for reviewing instructions, searching existing data sources, gathering and maintaining the data needed, and completing and reviewing the collection of information. Send comments regarding this burden estimate or any other aspect of this collection of information, including suggestions for reducing this burden, to Department of Defense, Washington Headquarters Services, Directorate for Information Operations and Reports (0704-0188), 1215 Jefferson Davis Highway, Suite 1204, Arlington, VA 22202-4302. Respondents should be aware that notwithstanding any other provision of law, no person shall be subject to any penalty for failing to comply with a collection of information if it does not display a currently valid OMB control number.
PLEASE DO NOT RETURN YOUR FORM TO THE ABOVE ADDRESS.

1. REPORT DATE *(DD-MM-YYYY)* 01-06-2022	**2. REPORT TYPE** Technical Memorandum	**3. DATES COVERED** *(From - To)* 6/2021-6/2022		

4. TITLE AND SUBTITLE A Method for Measuring Optical Distortion in Curved Optical Surfaces using Moiré Interferometry	**5a. CONTRACT NUMBER**
	5b. GRANT NUMBER
	5c. PROGRAM ELEMENT NUMBER
6. AUTHOR(S) Mark A. Nurge and Robert C. Youngquist and Annelisa B. Esparza	**5d. PROJECT NUMBER**
	5e. TASK NUMBER
	5f. WORK UNIT NUMBER

7. PERFORMING ORGANIZATION NAME(S) AND ADDRESS(ES) NASA Kennedy Space Center John F. Kennedy Space Center, Florida 32899	**8. PERFORMING ORGANIZATION** **REPORT NUMBER** L–

9. SPONSORING/MONITORING AGENCY NAME(S) AND ADDRESS(ES) National Aeronautics and Space Administration Washington, DC 20546-0001	**10. SPONSOR/MONITOR'S ACRONYM(S)** NASA
	11. SPONSOR/MONITOR'S REPORT **NUMBER(S)** NASA/TM–20220006738

12. DISTRIBUTION/AVAILABILITY STATEMENT

Unclassified-Unlimited
Subject Category
Availability: NASA STI Program (757) 864-9658

13. SUPPLEMENTARY NOTES

An electronic version can be found at http://ntrs.nasa.gov.

14. ABSTRACT

In FY2020, KSC's Applied Physics Lab created a computer based image processing system to allow inspection of the new visors being developed for the Artemis Program. This system was based on an ASTM standard where the distortion of an image is used to determine the optical aberrations in a visor, but this approach is restricted to small fields-of-view (small areas of the visor) and is limited in its ability to reliably detect and measure distortion. From our experience with flat surface inspection, we know that other optical techniques can offer higher sensitivity and accuracy. [1] This memorandum describes a method to model and measure the distortion in curved optical surfaces using moiré interferometry. We were able to apply this process to examine samples of the xEMU Artemis astronaut helmets. Design details are provided along with examples to illustrate performance.

15. SUBJECT TERMS

16. SECURITY CLASSIFICATION OF:			**17. LIMITATION OF** **ABSTRACT**	**18. NUMBER** **OF** **PAGES**	**19a. NAME OF RESPONSIBLE PERSON** STI Information Desk (help@sti.nasa.gov)
a. REPORT	**b. ABSTRACT**	**c. THIS PAGE**			
U	U	U	UU	44	**19b. TELEPHONE NUMBER** *(Include area code)* (757) 864-9658

Standard Form 298 (Rev. 8/98)
Prescribed by ANSI Std. Z39.18